KaryoTap Enables Cost-Effective High-Throughput Single-Cell Aneuploidy Profiling and Reveals How Positive and Negative Selection Shapes Cancer Genomes

Joseph C. Mays; josephcmays@gmail.com; Institute for Systems Genetics and Department of Biochemistry and Molecular Pharmacology, New York University Grossman School of Medicine, New York, NY 10016, USA; Current Address: Regeneron, 777 Old Saw Mill River Road, Tarrytown, NY 10591-6707

Fabio Alfieri; fabio.alfieri@nyulangone.org; Institute for Systems Genetics and Department of Biochemistry and Molecular Pharmacology, New York University Grossman School of Medicine, New York, NY 10016, USA

Maria Trifas; maria.trifas@nyulangone.org; Institute for Systems Genetics and Department of Biochemistry and Molecular Pharmacology, New York University Grossman School of Medicine, New York, NY 10016, USA

Manjunatha Kogenaru; manjunatha.kogenary@nyulangone.org; Institute for Systems Genetics and Department of Biochemistry and Molecular Pharmacology, New York University Grossman School of Medicine, New York, NY 10016, USA

Helberth M. Quysbertf; Helberth.Quysbertf@nyulangone.org; Institute for Systems Genetics and Department of Biochemistry and Molecular Pharmacology, New York University Grossman School of Medicine, New York, NY 10016, USA

Sally Mei; sallymei900@gmail.com; Institute for Systems Genetics and Department of Biochemistry and Molecular Pharmacology, New York University Grossman School of Medicine, New York, NY 10016, USA

Nazario Bosco; nazario.bosco.phd@gmail.com; Institute for Systems Genetics and Department of Biochemistry and Molecular Pharmacology, New York University Grossman School of Medicine, New York, NY 10016, USA. Current Address: Volastra Therapeutics, New York, NY 10027, USA.

Xin Zhao; Institute for Systems Genetics and Department of Biochemistry and Molecular Pharmacology, New York University Grossman School of Medicine, New York, NY 10016, USA

Joy Bianchi; joy.j.bianchi@gmail.com <joy.j.bianchi@gmail.com>; Institute for Systems Genetics and Department of Biochemistry and Molecular Pharmacology, New York University Grossman School of Medicine, New York, NY 10016, USA; Current address: Institute Pasteur, 25-28 rue du Dr Roux, 75724 Paris Cedex 15, France

Aleah Goldberg; Aleah.Goldberg@nyulangone.org; Institute for Systems Genetics and Department of Biochemistry and Molecular Pharmacology, New York University Grossman School of Medicine, New York, NY 10016, USA

Gururaj Rao Kidiyoor; Gururajrao.Kidiyoor@nyulangone.org; Institute for Systems Genetics and Department of Biochemistry and Molecular Pharmacology, New York University Grossman School of Medicine, New York, NY 10016, USA

Liam J. Holt; liam.holt@nyulangone.org; Institute for Systems Genetics and Department of Biochemistry and Molecular Pharmacology, New York University Grossman School of Medicine, New York, NY 10016, USA

David Fenyö; david.fenyo@nyulangone.org; Institute for Systems Genetics and Department of Biochemistry and Molecular Pharmacology, New York University Grossman School of Medicine, New York, NY 10016, USA

Teresa Davoli (corresponding author); teresa.davoli@nyulangone.org; Institute for Systems Genetics and Department of Biochemistry and Molecular Pharmacology, New York University Grossman School of Medicine, New York, NY 10016, USA

* equal contribution

Abstract

Aneuploidy—the presence of chromosome gains and losses—is highly prevalent in human tumors, yet the contribution of chromosome missegregation rates and selection to shape these patterns remains poorly understood. To address this challenge at scale, we developed KaryoTap, a cost-effective single-cell DNA sequencing method combining custom targeted panels for the Tapestri platform with a Bayesian gaussian mixture model to detect chromosome- and chromosome arm-scale aneuploidy as well as integrated gRNAs and barcodes. KaryoTap achieves an average accuracy of >85% for arm events and >90% for chromosome events at <$1 per cell, allowing scalable analysis of tens of thousands of cells per experiment. Through KaryoTap-based analysis of 11,555 cells, we performed in vitro evolution screens on immortalized human cells from mammary gland, pancreas and melanocytes. By comparing aneuploidy frequencies immediately after reversine-induced missegregation versus after extended proliferation, we quantified positive and negative selection for specific aneuploidies. Most aneuploidies—both gains and losses—are under negative selection, yet some chromosomal gains are under positive selection (such as 8q and 7q). We found that proliferative selective pressures can explain tissue-specific patterns of chromosomal gains observed in human cancers. *Critically, when positively selected events were excluded from analysis, correlations between in vitro and cancer gain frequencies strongly decreased or disappeared, whereas excluding negatively selected events largely preserved these correlations.* These findings demonstrate that proliferative selection shapes the landscape of chromosomal gains in cancer, with a more prominent role for positive selection.

Keywords

Aneuploidy, Chromosomal Instability, Single-Cell DNA Sequencing, Targeted DNA Sequencing, Cancer genomics, Tumor heterogeneity, Copy Number Variants, CNVs

Introduction

A critical hallmark of cancer initiation and progression is the presence of aneuploidy, or gains and losses of whole chromosomes or chromosome arms, which arise due to mitotic missegregation events(1–3). In addition to aneuploidy, chromosomal instability, characterized by a continuously high rate of these missegregation events among tumor cells, is a driver of tumor progression and metastasis(4,5). Chromosomal instability produces cell populations with heterogeneous aneuploid karyotypes that continuously evolve over time, granting tumor cells an opportunity to adapt to their environment and develop resistance to cancer therapies(6–8). Cancer aneuploidy is characterized by non-random patterns in which specific chromosomes are frequently gained or lost, while others remain largely unchanged. These patterns are often tissue-specific, with certain chromosomal alterations being common in some tumor types but rare or absent in others.

The genomic patterns of aneuploidy in cancer reflect both the frequency at which specific chromosomal alterations occur and the selective pressures that determine their persistence during tumor evolution (58-59, 68). Intrinsic genomic features influence the baseline rate of chromosome missegregation: chromosome size has been proposed to affect the probability of segregation errors, with larger chromosomes potentially experiencing higher rates of missegregation (59). In contrast, selective pressures shape which aneuploidies are retained, as the cumulative effects of oncogenes, tumor suppressor genes, and essential genes on each chromosome determine the fitness consequences of gains and losses in a tissue-specific manner (58, 67). While selection clearly plays an important role in shaping cancer aneuploidy patterns, the relative contributions of positive versus negative selection remain unclear. Recent computational analyses using machine learning approaches have suggested that negative selection may play a greater role than positive selection in shaping these patterns, with tumor suppressor gene density being a better predictor of chromosomal gain patterns than oncogene density (69). However, direct experimental evidence distinguishing between the contributions of missegregation

frequency and selective pressures—and between positive and negative selection—in human cells remains limited.

Traditional methods for detecting aneuploidy, such as whole genome sequencing (WGS), rely on bulk averaging of cell populations, effectively masking heterogeneity among individual cells and preventing assessment of the extent or rate of chromosomal instability. Single-cell approaches, particularly single-cell DNA sequencing (scDNA-seq), overcome this limitation(9–13). These data can be used to reassemble the karyotypic evolution of the tumor cells, which can provide insights into how aneuploidy and chromosomal instability drive tumorigenesis and inform treatments for therapeutic resistance(8,11). Methods for modeling aneuploidies of specific chromosomes in cell culture have also emerged as powerful tools for studying the effects of aneuploidy in cancer(14–16). These methods have benefitted from scDNA-seq, as sequencing individual cells enables the evaluation of the specificity and accuracy of the engineered karyotypes(15,16).

Single-cell DNA sequencing (scDNA-seq) methods have emerged as powerful tools for detecting aneuploidy in individual cells, though each approach involves tradeoffs between throughput, sensitivity, and cost (17–24). For scDNA-seq methods based on untargeted whole-genome sequencing (WGS), there is an inherent bias in the sensitivity of detecting whole-chromosome or arm-level gains and losses. Because sequencing reads are distributed proportionally across the genome, smaller chromosomes receive fewer reads than larger ones and are thus detected with lower sensitivity. However, when quantifying aneuploidy or chromosomal instability - defined as the rate of chromosome missegregation – each chromosome is counted as a single unit regardless of its size. Therefore, to achieve uniform sensitivity across all chromosomes, WGS-based scDNA-seq requires high sequencing depth, which increases cost substantially.

140 To address the need for a high-throughput, high-sensitivity, cost-effective method for detecting
141 chromosome-scale aneuploidy across the human genome, we turned to the Tapestri platform from
142 Mission Bio, a droplet-based targeted scDNA-seq solution that allows for the sequencing of hundreds of
143 genomic loci across thousands of cells in one experiment(25). The platform is commonly used to detect
144 tumor hotspot mutations in cancer driver genes, yet it has not been utilized to identify aneuploidy across
145 the genome. While targeted sequencing is typically used to identify single nucleotide mutations(26), we
146 reasoned that we could use the relative sequencing depth of targeted loci to detect chromosome- and
147 chromosome arm-scale aneuploidy in individual cells. Here, we describe KaryoTap, a cost-efficient
148 method combining custom targeted Tapestri panels of PCR probes covering all human chromosomes
149 with a Gaussian mixture model framework for DNA copy number detection, thus enabling the accurate
150 detection of aneuploidy in thousands of heterogeneous cells. Additionally, we included probes that detect
151 lentiviral-integrated CRISPR guide RNAs to enable functional studies and DNA barcodes to enable
152 sample multiplexing. This method also enables detection of copy number neutral loss of heterozygosity
153 (CNN-LOH) events due to its high sequencing depth. To enhance usability, we also developed a
154 companion software package for R, *karyotapR*, which enables the streamlined copy number analysis,
155 visualization, and exploration of the data produced by our custom panels. By overcoming the limitations
156 of current methods, this system will be a valuable tool for investigating the evolution and consequences
157 of aneuploidy and chromosomal instability in human tumors, in addition to other healthy and diseased
158 tissues.
159 Using KaryoTap, we conducted *in vitro* single-cell proliferation-based karyotype screens using different
160 types of immortalized untransformed human cells. Following treatment with an MPS1 inhibitor to induce
161 chromosomal instability and random aneuploidies, we allowed the cells to proliferate in culture over
162 several weeks. We observed that the patterns of chromosomal gains that emerged during *in vitro*
163 proliferation closely mirrored the aneuploidy patterns observed in human cancers. In contrast, the
164 patterns of chromosomal losses seen in tumors were not recapitulated *in vitro,* suggesting that the *in vivo*
165 tissue microenvironment may play a critical role in shaping these specific aneuploidy events *in vivo*.

166 These experiments demonstrate that Karyo-Tap is a powerful approach for uncovering the selective
167 forces that shape karyotype evolution in cancer and other biological contexts.

168 **Results**

169 ***Design of a Custom Targeted Panel for Detecting Chromosome-Scale Aneuploidy***

170 To enable accurate, cost-effective detection of aneuploidy at scale in thousands of single cells, we
171 designed custom targeted panels for the Tapestri system. Our Version 1 panel (v1; **Fig 1**; CO261) is
172 comprised of 330 PCR probes that target and amplify specific loci across all 22 autosomes and the X
173 chromosome (**Fig 1B**; **Table S1**; **Additional File 1**). The number of probes targeting each chromosome
174 was proportional to chromosome size (e.g., 24 probes for chr1, 5 for chr22) to achieve a roughly uniform
175 density of ~1-2 probes per gigabase across all chromosomes. Loci were selected to cover regions
176 carrying single nucleotide polymorphisms (SNPs) with major allele frequencies of 0.5-0.6 such that cells
177 from different lines or individuals sequenced in the same experiment could be identified by their distinct
178 genotypes. This is a key feature of our methodology compared to other scDNA-seq methods, as it allows
179 detection of loss of heterozygosity (LOH) including copy number-neutral LOH.

180 ***Population-Level Validation of KaryoTap Copy Number Estimates***

181 To validate that KaryoTap accurately detects chromosomal copy numbers, we pooled five cell lines with
182 distinct karyotypes and analyzed 2,986 cells in a single experiment. The pool consisted of near-diploid
183 RPE1 (+10q, XX)(6,27) as a reference population and four aneuploid colon cancer cell lines: LS513 (+1q,
184 +5, +7, +9, +13, +13, XY), SW48 (+7, +14, XX), LoVo (+5p, +7, +12, XY), and CL11 (-6, +7, +7, -17, -18,
185 -22, XY). Known karyotypes were confirmed by bulk WGS (**Fig S1A**) and G-banded karyotyping for RPE1
186 (**Fig S1B**).

187 Dimensionality reduction of variant allele frequencies (VAFs) by PCA and UMAP revealed 5 distinct
188 clusters corresponding to each cell line (**Fig S1C**), demonstrating that multiplexed samples can be

189 resolved by genotype alone. We identified the RPE1 cluster by comparing mean VAFs to published deep
190 WGS data(28) (**Fig S1D-E**) and used these cells as the diploid reference for copy number estimation.
191 Cell-probe copy number scores were calculated as the ratio of normalized read counts to the median of
192 the RPE1 reference population, then smoothed across probes targeting each chromosome to generate
193 cell-chromosome scores (see Methods).

194 At the population level, copy number profiles matched the expected karyotypes from bulk WGS for all
195 five cell lines (**Fig S2A**). For example, averaged heatmaps correctly showed 3 copies of chromosome 7
196 in LS513, SW48, and LoVo, and 4 copies in CL11; monosomy of chromosome 6 in CL11; and single X
197 chromosomes in male cell lines. Importantly, unbiased clustering distinguished all five populations by
198 copy number alone (**Fig S2B**), mimicking the subclonal structure of a heterogeneous tumor(31). Further
199 clustering within LoVo cells revealed two subpopulations distinguished by exclusive gains in chr5p or
200 chr15q (**Fig S2C**), demonstrating KaryoTap's ability to detect clonal heterogeneity. While this confirms
201 KaryoTap's accuracy at the bulk level, accurate copy number calling in individual cells requires
202 accounting for cell-to-cell variability, which we address below.

203 ***Bayesian Gaussian Mixture Modeling Enables Accurate Integer Copy Number Calling in Single-***
204 ***Cell DNA Sequencing Data***

205 To account for intracellular variation in the distributions of copy number scores, we classified the scores
206 as integer copy number calls using a 5-component Gaussian mixture model (GMM)(30), where each
207 component represents a possible copy number value of 1-5 (**Fig S3A**). To train the GMM model, we used
208 the known copy number state of each chromosome in RPE1 cells and simulated the expected distribution
209 of copy number scores for each integer copy number (1–5) separately for each chromosome. These 5
210 simulated distributions represent the score profiles that would be observed if a chromosome had 1, 2, 3,
211 4, or 5 copies, and they serve as the component distributions for the Gaussian mixture model. We then
212 applied Bayes theorem to calculate the posterior probability of each cell-chromosome score belonging to

213 each of the 5 GMM component distributions and assigned the cell-chromosome an integer copy number
214 corresponding to the component with the highest posterior probability (**Fig. S3A**; see Methods).

215 To evaluate copy number calling performance, we determined the accuracy of the classifier model,
216 calculated as the proportion of calls that were correct (i.e., true positives), using the known copy numbers
217 for RPE1 as ground truth on data generated using **KaryoTap Version 1** Panel. We focused on RPE1
218 as its karyotype is stable and homogeneous across the population(6); karyotyping confirmed that the line
219 is triploid for chr10q and diploid for all other chromosomes in all metaphases analyzed, with the exception
220 of 3 copies of chr12 in 3% of metaphases (**Fig S1B**). Accuracy, or correctly identifying 2 copies of a
221 chromosome in RPE1, varied between chromosomes and ranged from 95% for chr2 to 49% for chr22
222 with a mean of 79% (**Fig S3B**). Five-fold cross-validation confirmed robustness of these estimates (mean
223 absolute deviation: 0.61 to 4.75 percentage points across chromosomes). Eighteen out of 22
224 chromosomes had sensitivities of at least 75%; chr10 was excluded from whole-chromosome analysis
225 because the p and q arms have different copy numbers. Accuracy for each chromosome correlated
226 strongly with chromosome length (Pearson r = 0.73), and chromosome length itself correlated strongly
227 with the number of probes targeting the chromosome (Pearson r = 0.93) (**Fig S3C**), suggesting that
228 classifier accuracy is related to the number of probes targeting a chromosome. As expected, linear
229 regression of accuracy on the number of probes per chromosome indicated that the number of probes is
230 predictive of copy number call accuracy (R^2 = 0.76; p = 1.12e-08) (**Fig S3D-E**). We next performed a
231 similar analysis for chromosome arms (**Fig S4A**). We called integer copy numbers using a GMM
232 generated for each chromosome arm and evaluated classifier accuracy for correctly calling copy numbers
233 in RPE1. The arm-level accuracy ranged from 91% (chr2q) to 50% (chr19p, chr22q) with a mean of 69%
234 (**Fig S4B**). Twenty-two out of 41 arms had accuracy values of at least 70%. A positive relationship
235 between the number of probes and accuracy was again confirmed by linear regression (R^2 = 0.59; p =
236 5.1e-09) (**Fig S4C**). Overall, our system accurately calls copy numbers for the majority of chromosomes

237 and chromosome arms, with lower accuracy for smaller chromosomes and arms and that classifier
238 accuracy could be improved by adding additional probes (see also **Supplemental text**).

239 ***Impact of Probe Number and Sequencing Depth on Accuracy***

240 We performed extensive simulation-based analyses to characterize the parameters influencing copy
241 number classification accuracy; full details are provided in the **Supplemental Text** and summarized here.
242 Briefly, probe downsampling experiments on chromosomes 2 and 6 confirmed that probe number, not
243 chromosome size, drives classification accuracy, with median accuracy decreasing substantially as
244 probes were reduced from full coverage to 4 probes per chromosome (**Fig S2D**). Variability in accuracy
245 also increased markedly with fewer probes (**Fig S3A**). Panel simulations using 120 probes from
246 chromosomes 1–6 demonstrated that mean theoretical sensitivity increases with probe number across
247 all copy number levels (**Fig S2E**), achieving ≥90% sensitivity at 4 probes for losses, 20 for diploid states,
248 and 50 for 3-copy gains. A simpler 3-component GMM (loss/neutral/gain) achieved ≥90% sensitivity at
249 26 probes for gains, with 99% sensitivity requiring 76 probes (**Fig S3B**). In contrast, sequencing depth
250 had modest effects: downsampling from 85 to 17 reads per cell per probe decreased sensitivity by only
251 4.4 percentage points (**Fig S2F**), indicating that probe number remains the dominant factor while depth
252 beyond ~35 reads provides minimal additional benefit.

253 ***KaryoTap Version 3 Panel Increases Accuracy of Aneuploidy Detection to ~90% Keeping the Cost***
254 ***per Cell at a Minimum***

255 As the accuracy of our custom panel increases with the number of probes targeting a chromosome, we
256 optimized our design by adding probes to chromosomes with lower coverage. To balance cost with
257 meaningful sensitivity gains, we removed the 61 least efficient probes (by total read counts) and added
258 82 probes such that each chromosome was targeted by at least 12 probes (**Table S1**). We also included
259 4 probes targeting chrY, enabling detection of all 24 chromosomes (**Fig S6A**). The new panel, Version 2

260 (v2; CO610) comprises 352 total probes, 270 of which are shared with v1 (**Fig 1B**; Additional File 2). To
261 further improve arm-level accuracy, we modified v2 to generate **Version 3** (v3; CO810; **Fig 1B**; Additional
262 File 3). V3 includes 399 total probes, 309 shared with v2, prioritizing chromosome arms with lower
263 coverage. The barcode and gRNA-detecting probes were retained in both designs.

264 To evaluate v2 and v3 performance, we performed a Tapestri experiment using RPE1 cells (**Fig S6B**)
265 and determined empirical sensitivity as the proportion of cells with correct copy number calls. Five-fold
266 cross-validation confirmed robustness (MAD: 0.49 to 4.74 pp for v2; 0.60 to 3.31 pp for v3). The poorest
267 performing chromosome in v1, chr22, had sensitivity of 62% with v2 (**Fig S6C**) and 78% with v3 (**Fig 2A**),
268 compared to 46% for v1 (**Fig S3B**). Mean sensitivity across all chromosomes was 85% for v2 (**Fig S6C**)
269 and 91% for v3 (**Fig 2A-B**), increased from 79% for v1. Accuracy increased by 2.2 pp on average for
270 each additional probe (**Fig 2C**). Similarly, arm-level average sensitivity increased from 69% (v1) to 76%
271 (v2; **Fig S6D**) to 83% (v3; **Fig 2D-E**), with 2.9 pp improvement per additional probe. Theoretical sensitivity
272 also improved across panels for both 5-component and 3-component GMMs (**Fig S7A**). The decreased
273 noisiness in heatmaps of GMM copy number calls across v1, v2, and v3 for RPE1 (**Fig 2F**), LoVo (**Fig**
274 **2G**), and LS513 (**Fig 2H**) further supports improved accuracy with v3. Altogether, panel v3 delivers
275 accurate copy number calls in thousands of single cells with arm-level resolution.

276 The main purpose of KaryoTap is to detect chromosomal instability and aneuploidy at the chromosome
277 level. In scDNA-seq methods based on untargeted WGS (e.g., Arc-well, 60), sensitivity of aneuploidy
278 detection depends on total reads per chromosome and thus is inherently lower for smaller chromosomes.
279 For evaluating aneuploidy and chromosomal instability, each chromosome counts as a single entity
280 regardless of size. Thus, WGS-based scDNA-seq methods require high read depth—and higher cost—
281 to achieve sufficient sensitivity across all chromosomes. KaryoTap experiments cost approximately $0.5-
282 1 per cell—less than 10% of alternative methods (see also Supplemental Text). By achieving comparable
283 detection sensitivity at a fraction of the cost compared to WGS methods, KaryoTap provides a scalable

284 and cost-effective solution for high-throughput aneuploidy detection that overcomes the size-dependent
285 biases inherent to WGS-based approaches.

286 **Detection of Lentiviral Barcodes and gRNAs Allows for Genetic Screenings: Example of**
287 **KaryoCreate-based Screen for Centromeric sgRNAs**

288 To extend the capabilities of our system for functional genomics, we added two probes to the Version 2
289 panel that target and amplify either a DNA barcode sequence or CRISPR guide RNA (gRNA) sequence
290 integrated into a cell's genome by lentiviral transduction. DNA barcoding can be used when several
291 samples from the same cell line or individual are sequenced together and cannot be distinguished by
292 genotype. Similarly, CRISPR gRNAs can be used both for functional studies and as barcodes
293 themselves, indicating the gRNA treatment received by each individual cell.

294 As proof-of-concept, we transduced RPE1 cells and human colorectal epithelial cells (hCECs) each with
295 distinct gRNA constructs (gRNA1 and gRNA2, respectively), and human Pancreatic Nestin-Expressing
296 cells (hPNEs) with a mix of two DNA barcode constructs that drive BFP expression. We used distinct cell
297 lines for each construct so the three populations could be distinguished by genotype without assuming
298 successful barcoding. Probe AMP350 targets the region surrounding and including the gRNA sequence
299 in the lentiviral vector; Probe AMP351 targets the barcode sequence region (**Fig 3A**).

300 gRNAs were transduced at a multiplicity of infection (MOI) of 1-1.5 with puromycin selection; BFP
301 barcodes were transduced at higher MOI with FACS enrichment for BFP expression. The three
302 populations were pooled and analyzed in a single Tapestri experiment using panel Version 2, with
303 populations distinguished by PCA, UMAP, and clustering of VAFs (**Fig S6B**). RPE1 cells had an average
304 of 34 gRNA1 reads per cell (0 in other lines), hCECs had 30 gRNA2 reads per cell, and hPNEs had 81
305 barcode reads per cell (**Fig 3B**). Detection rates were 79% for RPE1 gRNA1, 69% for hCEC gRNA2, and
306 94% for hPNE barcodes (**Fig 3B**), with virtually all probe reads matching expected sequences (**Fig S7B**),

307 indicating high specificity with no contamination. Detection rates can be further improved through higher
308 MOI transduction or increased sequencing depth.

309 To demonstrate the combined copy number detection and multiplexing capabilities of our system, we
310 tested it on samples treated with KaryoCreate (Karyotype CRISPR Engineered Aneuploidy Technology),
311 our method for inducing chromosome-specific aneuploidy in cultured cells(14). KaryoCreate uses
312 CRISPR gRNAs to target a mutant KNL1-dCas9 fusion protein to the centromere of a specific
313 chromosome, causing missegregation in ~20% of cells. KaryoTap represents an ideal method to evaluate
314 the efficiency and chromosome-specificity of KaryoCreate. We performed a Tapestri experiment on
315 hCECs treated with gRNAs previously tested using KaryoCreate: sgNC (untargeted negative control),
316 sgChr6-2 (targets chr6), and sgChr7-1 (targets chr7). The gRNA sequences amplified by AMP350 were
317 used to identify the gRNA each cell received.

318 sgChr6-2 and sgChr7-1 induced gains and losses specifically in intended chromosomes, but not others,
319 compared to sgNC (**Fig 3C**, **Table S2**; $p < 0.001$, Fisher's exact test). sgChr6-2 induced 26.6% losses of
320 chr6 compared to 0.5% with sgNC, and 8.3% gains compared to 2.0% (**Table S6**). sgChr7-1 induced
321 6.1% losses of chr7 compared to 0.5% with sgNC, and 5.1% gains compared to 4.3%.

322 In the same experiment, we screened 5 sgRNAs targeting chromosome 20 (sgChr20-2, 20-3, 20-4, 20-
323 6, and 20-7) that were previously described but not validated by imaging (14). Chromosome 20 is one of
324 the most frequently gained chromosomes in human cancer(2), but its small size and low number of
325 centromeric gRNA binding sites (~700) had prevented validation by imaging or scRNA-seq. sgChr20-2,
326 20-4, 20-6, and 20-7 did not induce changes in chr20 ($p = 0.557$-0.926). However, sgChr20-3 induced
327 11.1% gains in chr20 compared to 6.0% with sgNC, and 5.7% losses compared to 4.0% ($p = 0.012$).
328 Notably, sgChr20-3 also induced 9.4% losses and 18.5% gains in chr2 ($p < 0.001$). The sgChr20-3
329 sequence (GGCAGCTTTGAGGATTTCGT) matches 18 out of 20 base pairs for loci on the chr2
330 centromere (GATAGCTTTGAGGATTTCGT)(14), suggesting an explanation for this off-target effect.

331 These data indicate that KaryoTap successfully enables simultaneous detection of aneuploidy and
332 gRNA/barcodes in the same cells and thus can be used to perform CRISPR-based (i.e., gRNA-based)
333 or ORF-based (barcode-based) functional screens.

334 ***Karyotap Enables Detection of Copy Neutral Loss of Heterozygosity (CNN-LOH)***

335 Gains and losses of diploid chromosomes result in a shift in VAF for their heterozygous SNPs from 50%
336 in the direction of 100% or 0% depending on which parental chromosome copy (i.e., haplotype)
337 experienced a copy number change. In addition, a shift in VAF can also be observed in the absence of
338 copy number changes in copy number neutral loss of heterozygosity (CNN-LOH), which has been
339 observed in cancer as well as normal tissues. Because each probe is sequenced at a high depth,
340 KaryoTap is able to detect this shift, allowing us to determine which of the two parental
341 chromosomes/haplotypes was gained or lost. This is especially important for detecting loss of
342 heterozygosity (LOH), a common event in cancer whereby a heterozygous-to-homozygous shift by
343 chromosomal loss can inactivate tumor suppressor genes(31,32, 71). To determine if KaryoTap could
344 detect allele frequency shifts following chromosomal gains and losses, we examined the cells from the
345 KaryoCreate experiment (**Fig 3A**) that had lost a copy of chromosome 6 after treatment with the sgChr6-
346 2 gRNA. We identified 9 heterozygous variants on chr6 by identifying variants with a mean allele
347 frequency between 20-80% in the sgNC control population. We then calculated a relative (i.e., haplotype-
348 agnostic) allele frequency for sgChr6-2 treated cells with 1 or 2 copies of chr6 by calculating the absolute
349 difference between raw allele frequency and 50% such that 0 corresponded to heterozygous alleles and
350 50 corresponded to fully homozygous alleles (**Fig 3D**). 4 distinct clusters of cells emerged using K-means
351 clustering on relative AFs. The cluster comprising cells with a copy number call of 2 for chr6 shows that
352 the 9 variants are heterozygous in diploid cells as expected. The cluster with one copy of chr6 shows a
353 shift across the variants from heterozygous to homozygous (i.e. a loss of heterozygosity), supporting the
354 loss of one copy of each allele in these cells. There are also two smaller clusters representing the loss of
355 either chromosome arm but not the other, supported by both the loss of heterozygosity in the variants on

356 the affected arm and the copy number call of 1 for that arm (**Fig 3D**). This indicates that KaryoTap can
357 be used to detect loss of heterozygosity in single cells at the population level.
358
359 It is possible that the loss of a chromosome can be followed by a duplication of the remaining
360 chromosome, such that the copy number of the chromosome remains the same, but one allele is lost,
361 i.e., a CNN-LOH. To determine if KaryoCreate can cause CNN-LOH in the targeted chromosome, we
362 took the relative allele frequencies for sgChr6-2 treated cells with 1 or 2 copies of chr6 calculated above
363 and averaged them such that each cell had one mean relative AF value for chr6. We also repeated this
364 calculation for the cells treated with the sgNC control gRNA. If we consider relative AF between 40% and
365 50% to indicate homozygosity of chr6 alleles and 0% to 40% to indicate heterozygosity, all sgNC-treated
366 cells with a chr6 copy number of 2 were heterozygous (**Fig 3E**). Cells that lost a copy of Chr6 following
367 treatment with sgChr6-2 were detected to be homozygous for their remaining allele. 85% of cells treated
368 with sgChr6-2 that had 2 copies of chr6 detected were heterozygous, while 15% were detected as
369 homozygous, indicating a loss of heterozygosity with no change in the net copy number in this population
370 (2 copies of chr6). This indicates that KaryoCreate can induce CNN-LOH, and KaryoTap can detect CNN-
371 LOH events.

372 ***KaryoTap enables single cell-based screens to differentiate between occurrence rate and***
373 ***selection among chromosomal gains and losses***

374 We next utilized KaryoTap to perform a karyotype evolution screening with the goal of assessing whether
375 the gain or loss of any chromosome or chromosome arm would confer a fitness advantage or
376 disadvantage during cellular proliferation *in vitro*. Given its resolution and scalability, KaryoTap is well-
377 suited for monitoring how aneuploidy patterns occur and are selected under proliferative pressure. To
378 model aneuploidy induction and selection , we exposed nontransformed, near-diploid cell lines to
379 Reversine (an MPS1 inhibitor) to induce chromosomal missegregation and thus gains and losses of all
380 chromosomes (74) (**Fig 4A**). By profiling cells immediately after Reversine exposure and again after

381 several weeks in culture, we monitored how initial random aneuploidy events are progressively filtered
382 by positive and negative selective pressures.

383 Three near-diploid hTERT immortalized cell lines - hPDE (Human Pancreatic Duct Epithelial), hMEL
384 (Human Melanocyte), and hMEC (Human Mammary Epithelial) - were used for this screen upon labeling
385 them with a unique DNA barcode enabling demultiplexing (**Fig S8**). These cell lines were subjected to
386 treatment with DMSO (control) or two concentrations of Reversine (75 nM and 150 nM) for up to 48 hours.
387 Following Reversine treatment, cells were allowed to recover, and on the second day post-release
388 (hereafter referred to as Day 2), a subset of cells was harvested and prepared for sequencing. This early
389 timepoint provides an initial snapshot of the chromosomal landscape shortly after drug exposure. Cells
390 were then cultured under standard conditions for an extended period of approximately 28 days, allowing
391 evolutionary dynamics to unfold (**Fig 4A**). This later timepoint will be referred to as Day 28.

392 On Day 2, both 75 nM and 150 nM Reversine concentrations resulted in high levels of chromosome- and
393 chromosome-arm gains and losses compared to the DMSO control, indicating that aneuploidy events are
394 initially increased in response to Reversine treatment (**Fig 4B-D**). The total aneuploidy frequency (gains
395 and losses) appeared to disproportionately involve larger chromosomes at Day 2, as suggested by
396 significant positive correlations between normalized aneuploidy frequencies and chromosome size
397 across all tested lines (**Fig 4E-G**). This indicates that chromosome size is an important factor in
398 determining the likelihood that a chromosome undergoes missegregation. Notably, despite the observed
399 positive correlations with chromosome size, we did not observe a similar trend for centromere size (**Fig**
400 **S9**), indicating that shortly after the induction of missegregation through Reversine (Day 2), chromosome
401 size rather than centromere size drives the bias toward chromosomal gains and losses. However, by Day
402 28, this correlation was notably reduced or absent in all tested cases, coupled with an overall decrease
403 in aneuploidy levels in both treatment groups across all tested cell lines (**Fig 4H-J**). At Day 28, a
404 significant reduction in the average number of gains and losses per cell was observed compared to Day

405 2 (**Fig 4B-D**). These findings underscore the presence of strong negative selective pressures acting
406 against aneuploidy during prolonged *invitro* culture, favoring the restoration of genomic stability.

407 ***Estimation of positive and negative selection on chromosomal gains and losses during cell***
408 ***proliferation***

409 We aimed to utilize the frequencies of chromosome arm gains and losses at Day 2 and Day 28 to estimate
410 whether their events were under positive or negative selection during in vitro proliferation. All analyses
411 were performed at the chromosome-arm level, which represents the highest resolution achievable with
412 KaryoTap and allows detection of both whole-chromosome and arm-level events. To quantify the
413 magnitude of selection acting on gains and losses in each cell line, we computed chromosome arm
414 selection scores. For each arm and event class (gain or loss), we performed a Fisher's exact test to
415 compare the Day 28 to Day 2 frequencies to derive a selection score. Selection scores were defined as
416 the log2 odds ratio: positive (gain or loss) selection scores indicate enrichment of the event at Day 28
417 relative to Day 2 (positive selection), whereas negative values indicate depletion of the event at Day 28
418 relative to Day 2 (negative selection) (**Fig 5A-C, S10**, see also **Methods**). This framework accounts for
419 both cell line-specific, pre-existing aneuploidies and chromosome-size-dependent missegregation
420 frequencies, isolating and quantifying selection during the outgrowth phase.

421

422 Overall, the majority of chromosome-arm copy-number events were classified as negatively selected
423 across all conditions (**Fig 5A-I**). For example, the frequency of chromosome 8q loss decreased
424 significantly from Day 2 to Day 28 in hMECs (from 21% at Day 2 to 2% at Day 28, **Fig 5G**); similarly
425 chromosome 1q gain decreased from Day 2 to Day 28 in hMECs (from 19% at Day 2 to 7% at Day 28,
426 **Fig 5G**). Despite widespread negative selection, a few events were also classified as positively selected
427 (80 under negative and 12 positive across all lines), such as 8q gain in hMEL and hMEC, (respectively
428 from 11% and 12% at Day 2 to 28% and 18% at Day 28, Fig. 5G, I); or 7q gain in hPDE (from 2% at Day
429 2 to 9% at Day 28, **Fig. 5H**). Overall, events under negative selection were dominated by losses (~60%

430 of negatively selected events were losses) while events under positive selection were for the vast majority
431 gains (~80% of them). In line with this asymmetry, losses exhibited a significantly lower frequency at Day
432 28 than Day 2 (**Fig 5G-I** and **Fig S10**).
433
434 Across the three epithelial lineages, we observed both common and cell type-specific selection
435 landscapes. In hMEC and hMEL, but not hPDE, (**Fig 5A**), 8q gain was under strong positive selection. In
436 addition, in hMEC there was significant negative selection for tissue-specific chromosome arm gains,
437 such as 9p, while most of the other chromosome arms showed negative selection for both gains and
438 losses. In hPDE (**Fig 5B**), 7q shows strong positive selection for gains and negative selection for losses,
439 while 3q and 6q show strong negative selection for gains and positive selection for losses. hMELs (**Fig**
440 **5C**) show significant positive selection for gains in 8q and negative selection for gains in 2q, 6p, 13q, and
441 18q, and strong negative selection against losses in 1q, 7q, 17q, and 19p.
442
443 One notable example of common positive selection across multiple cell lines is 8q gain in both hMEC
444 and hMEL cells, which showed a significant increase in frequency from Day 2 to Day 28 compared to the
445 diploid state, suggesting that this event confers a proliferative advantage in both these cell types.
446 Knowing the frequency at Day 2 and Day 28, along with their doubling times, we were able to estimate
447 the fitness advantage conferred by 8q gain in these cell lines, deriving a selection coefficient of 0.0624
448 for hMEL and 0.0133 for hMEC (see **Methods**). These selection coefficients demonstrate tissue-specific
449 fitness advantages conferred by 8q gain during in vitro proliferation. The nearly five-fold stronger selection
450 in hMEL cells compared to hMEC cells indicates that identical chromosomal alterations can provide
451 markedly different proliferative advantages depending on cellular context. While 8q is recurrently gained
452 in both melanoma and breast cancer, our quantitative measurements suggest that its fitness contribution
453 varies substantially across tissue types, potentially reflecting differences in the baseline expression or
454 functional importance of 8q-resident genes like MYC in different epithelial lineages. Altogether, these

455 analyses indicate that most aneuploidies – both gains and losses – are subject to negative selection
456 during in vitro proliferation, with notable exceptions such as 8q gain and 7q gain.

457 ***KaryoTap reveals that selection shape the patterns of gains observed in human cancer patient,***
458 ***with a more prominent role for positive selection***

459 To investigate whether chromosomal evolution under experimental in vitro conditions reflects aneuploidy
460 patterns observed in human cancers, we compared the chromosome-arm gain frequencies from TCGA
461 (BRCA, PAAD, SKCM, and Pan-cancer) to the normalized Reversine-treatment gain frequencies (defined
462 as the frequency in Reversine-treated cells over DMSO control), at both Day 2 and Day 28. Specifically,
463 we asked whether the chromosome-arm aneuploidy observed in hMEC, hPDE, and hMEL cells over time
464 would recapitulate the gain patterns characteristic of breast cancer (BRCA), pancreatic adenocarcinoma
465 (PAAD), and skin cutaneous melanoma (SKCM), respectively, as well as in a pan-cancer analysis. The
466 scatterplots in **Fig 5J-O** show the comparison between experimental gain frequencies and the
467 corresponding TCGA gain frequency for each tissue at Day 2 (J-L) and Day 28 (M-O).

468 At Day 2, there was no significant correlation between the chromosome-arm gain frequencies in TCGA
469 samples (BRCA, PAAD, SKCM, and Pan-cancer) and those observed in the matched *in vitro* counterparts
470 (hMEC, hPDE, and hMEL). This indicates that the immediate effects of Reversine induce aneuploidy in
471 a manner that does not mirror cancer-associated patterns, instead reflecting intrinsic missegregation
472 propensities of specific chromosomes (**Fig 4E-J**). By Day 28, however, we observed a partial
473 recapitulation of cancer-associated gain patterns: correlations between TCGA gain frequencies and the
474 corresponding *in vitro* gain frequencies significantly increased across tissues. For example, the
475 correlation between BRCA gain frequency and hMEC increased from −0.0069 at Day 2 (n.s.) to 0.33 at
476 Day 28 ($p < 0.05$). Similarly, hPDE increased from 0.16 (n.s.) at Day 2 to 0.46 ($p < 0.01$) at Day 28, and
477 hMEL from 0.13 (n.s.) at Day 2 to 0.27 ($p = 0.08$). This underscores the role of selection pressures that
478 emerge over time during culture, progressively shaping tissue-specific aneuploidy landscapes toward

479 cancer-like patterns. Notably, even at Day 28 the correlations, while significant, were moderate,
480 indicating that *in vitro* evolution only partially recapitulates the aneuploidy landscape found in cancers.
481 Moreover, these analyses focus on gains: we did not observe a similar recapitulation for losses (**Fig S11**;
482 see **Discussion**).

483 Finally, we asked whether it was primarily the events under positive or
484 negative selection that determined the significant correlation between the *in vitro* proliferation screen and
485 the frequencies observed in TCGA. To address this, we excluded the events that were identified as being
486 under positive or negative selection from the TCGA correlation analysis, as described
487 above. We observed that when excluding events under negative selection, the significant association
488 between the frequency of gains *in vitro* and in TCGA (Pancancer frequencies) remained intact across all
489 tested cell lines (hMEC Pearson's R from 0.33 to 0.51; hPDE Pearson's R from 0.46
490 to 0.42; hMEL Pearson's R from 0.27 to 0.25). However, strikingly, when excluding events under
491 positive selection, the positive association between the *in vitro* screen and TCGA
492 frequencies strongly decreased for all tested cell lines (hMEC Pearson's R from 0.33
493 to 0.064; hPDE Pearson's R from 0.46 to 0.32; hMEL Pearson's R from 0.27 to -0.042). **Overall, this**
494 **analysis suggests that positive selective pressure is a critical driving force shaping the patterns**
495 **of chromosomal gains observed in human tumors.**

496

497

498

499 **Discussion**

500

501 We designed custom panels for the Tapestri platform that enable targeted scDNA-seq of specific loci
502 across all human chromosomes, coupled with a GMM-based copy number calling analysis pipeline for
503 the identification of chromosome- and chromosome-arm-scale aneuploidy in thousands of cells with high
504 accuracy and at greatly reduced sequencing depth compared to single-cell WGS methods(17–19). To
505 increase ease-of-use, we compiled the computational scripts into an R package, *karyotapR*,
506 which facilitates copy number calling and visualization (**Fig S12**). Using KaryoTap, we conducted in vitro
507 proliferation screens that revealed how selection forces shape cancer genomes, demonstrating that
508 proliferative selective pressures explain chromosomal gain patterns observed in tumors, while losses
509 appear driven by non-proliferative cancer phenotypes. This easily adoptable, flexible, cost-efficient and
510 highly scalable system lays the groundwork for an innovative class of tools for studying aneuploidy and
511 chromosomal instability in healthy and diseased tissues and tumors.

512

513 While single-cell aneuploidy detection is not unique to KaryoTap, our design has several advantages, the
514 most critical being the ability to scale up throughput to thousands of cells in one experimental run, thus
515 significantly reducing hands-on time, reagent cost, and sequencing cost per cell. Additionally, targeting
516 of specific loci allows us to forgo the typical technical difficulties of conventional WGS analysis, including
517 correcting for mappability bias and GC bias, and the use of segmentation algorithms to make copy
518 number calls(26). Furthermore, the total number of sequencing reads needed to obtain high-accuracy
519 copy number calls for KaryoTap is greatly reduced compared to WGS-based scDNA-seq methods, and
520 the targeted nature of the assay spreads the reads more evenly across the genome, preventing the
521 biasing of detection sensitivity toward larger chromosomes that is seen with WGS. We expect this will be
522 particularly important for accurately assessing chromosomal instability as the smallest of chromosomes
523 will be more equally represented in the data relative to the larger chromosomes. Finally, the commercial
524 availability of the Tapestri system allows for easier adoption and reproducibility compared to non-

525 commercialized "homebrew" methods that need to be established and optimized in each lab from scratch
526 (22).
527
528 As evidenced by the analysis of RPE1, our method generates a range of smooth copy number
529 measurements for chromosomes with the same copy number, indicating some level of technical error.
530 To account for this error and convert the continuous smooth copy number scores to discrete copy number
531 values, we used a Gaussian mixture model (GMM) classification strategy, which has been previously
532 used for copy number analysis of single-cell whole genome sequencing data(34). This allows each
533 smooth copy number score to be associated with a set of (posterior) probabilities of being measured from
534 a chromosome of a given range of copy numbers (e.g., 1, 2, 3, 4, or 5). As the number of probes
535 increases, the variance of the model components decreases, resulting in an increase in classifier
536 accuracy that we observe between our iterative v1 to v3 panel designs. While we use a near-diploid cell
537 line as our ground truth, the GMM strategy also allows us to calculate the expected (theoretical) sensitivity
538 that a chromosome with copy number 1, 2, 3, 4, or 5 would be correctly called using our system by
539 calculating the proportion of overlap between the copy number components of the model. Further
540 improving the panel by increasing the number of probes will allow us to more confidently observe the
541 karyotype heterogeneity in these samples as well as in tumors and other tissues.
542
543 Deep sequencing (~80-100X on average per cell) of each target region allows for robust single nucleotide
544 variant (SNV) calling that is not possible at the lower genomic coverage afforded by other high-throughput
545 methods(22). This enabled us to resolve and identify 5 multiplexed cell lines in a single experiment by
546 clustering cells by variant allele frequencies. Since our panels specifically target loci known to harbor
547 SNPs across the human population, we can extend sample multiplexing to clinical samples (e.g., tumor
548 tissue) from different individuals without the need for barcodes, further reducing experimental costs.
549 Additionally, while our panels were designed for copy number analysis, additional probes could be added
550 that cover tumor suppressor genes and oncogenes of interest, thus revealing consequential point

551 mutations alongside chromosomal copy number. Mission Bio offers several ready-made panels covering
552 mutational hotspots and genes relevant to a broad range of tumor types, allowing for a great degree of
553 customizability. Furthermore, we demonstrated that SNV-associated allele frequency shifts detected
554 using KaryoTap could be used to infer loss of heterozygosity (LOH), a common event in cancer where
555 the germline heterozygous state of a chromosome changes to a homozygous state in tumor cells(33).
556 LOH has been demonstrated to promote tumorigenesis by inactivating tumor suppressor genes through
557 chromosomal loss(31,32). In the context of chromosomal instability, the chromosome remaining after the
558 loss of its homologue can be duplicated, resulting in LOH with a net-neutral copy number change (copy
559 number neutral (CNN)-LOH). The deep sequencing depth and copy number detection enabled by
560 KaryoTap allow for discovery of CNN-LOH events, which would otherwise be difficult to detect with the
561 shallow coverage typical of other scDNA-seq methods(33).
562
563 To enable experimental design flexibility when using our custom panels, we added a set of probes that
564 can detect DNA barcode and CRISPR gRNA sequences integrated into the genome. DNA barcodes can
565 be used to multiplex and resolve cells belonging to different samples in a single Tapestri experiment that
566 otherwise could not be distinguished by genotype. Through barcoding, users can compare samples from
567 the same individual or compare experimental and control conditions in the same cell lines while
568 minimizing batch effects. Regardless of design, combining several samples into one experimental run
569 greatly reduces the per-sample reagent and sequencing costs in addition to the hands-on time required
570 to process the samples. Detecting barcodes in thousands of cells is made possible by exploiting the
571 targeted nature of the sequencing assay. Single-cell DNA sequencing methods with comparable
572 throughput rely on inefficient and random transposon insertion, which would only detect a randomly
573 inserted barcode in about 20% of cells(22). By specifically targeting and selecting for the barcoded insert,
574 we can reliably recover the barcode sequence in over 90% of cells. Furthermore, including a probe that
575 targets inserted CRISPR gRNA sequences allows for an additional layer of experimental design flexibility
576 where the gRNA-mediated treatment that each cell receives can be identified by the gRNA sequence

577 itself. Here, we demonstrated the gRNA detection and multiplexing capabilities of our system by
578 evaluating the efficiency and specificity of KaryoCreate, our method for inducing chromosome specific
579 aneuploidy. Since the gRNAs can be detected in 70-80% of cells when transduced at low MOI, this
580 system could also be used for CRISPR screen applications where cells are randomly treated with one
581 gRNA from a library of hundreds of possible gRNAs and thus require high detection sensitivity(35).
582 Altogether we describe KaryoTap as a cost-effective, high-throughput single-cell DNA sequencing
583 method to detect chromosome-scale aneuploidy with high accuracy and enable functional genomic
584 screens through barcode/gRNA detection.
585 A fundamental question in understanding chromosomal instability is what structural parameters of
586 chromosomes determine their propensity for missegregation. Our data reveal a strong positive correlation
587 between chromosome size and missegregation frequency at Day 2 following Reversine treatment, with
588 larger chromosomes exhibiting higher rates of gains and losses across all three cell lines tested (**Fig 4E-**
589 **G**). Chromosome size is often associated with nuclear positioning, as larger chromosomes tend to occupy
590 more peripheral locations within the nucleus. A recent study demonstrated that nuclear chromosome
591 location dictates segregation error frequencies, with chromosomes in certain nuclear positions being
592 more prone to entrapment in micronuclei following error-prone mitosis (69). Our findings are consistent
593 with a model in which chromosome size—and its associated nuclear positioning—influences the
594 likelihood of missegregation during mitosis when missegregation is induced via MPS1 inhibitors. Notably,
595 we did not observe an association between centromere size and missegregation frequency (**Fig S7**) (65).
596 This discrepancy may reflect differences in the mechanisms of missegregation operating in different cell
597 and tissue types. Interestingly, gain of 1q, one of the most frequent events observed in our study (Figure
598 5), is also frequently found in the normal mammary gland; thus its presence in normal mammary tissue
599 may reflect both the frequency of occurrence and a potential selective advantage (70, 75).

600 Our study reveals that the majority of aneuploidies—both gains and losses—are subject to negative
601 selection during *in vitro* proliferation. While positive selection enriches specific chromosomal gains such

602 as 8q and 20q, the broader aneuploidy landscape is dominated by the elimination of deleterious
603 aneuploidies over time. By comparing our in vitro screen with primary tumor data, we observed that the
604 frequency of chromosomal gains at Day 28 (but not Day 2) significantly correlated with gain frequencies
605 in matched TCGA cancer types. Most importantly, when we excluded chromosomal events identified as
606 being under positive selection, these correlations decreased or disappeared, whereas excluding
607 negatively selected events mostly preserved the TCGA associations. This demonstrates that the patterns
608 of chromosomal gains observed in human cancers are shaped predominantly by selective pressures
609 acting during proliferation, rather than by the intrinsic frequency of chromosome missegregation. The
610 convergence between our *in vitro* evolution screens and patient cancer genome landscapes thus reflects
611 shared selective advantages operating in both contexts. Collectively, these findings demonstrate that
612 proliferative selection shapes the landscape of chromosomal gains in cancer, with positive selection
613 exerting a more prominent influence than negative selection in determining the final aneuploidy patterns.
614 Interestingly, in a complementary study (77), computational inference of positive and negative selection
615 across cancer aneuploidy revealed that positive selection scores are positively associated with Day 28
616 gain frequencies, while negative selection scores are negatively associated with Day 28 gain frequencies.
617 In agreement with our findings, positive selection scores showed stronger correlations than negative
618 selection scores (77).

619 The chromosome 8q and 20q gains we observed under positive selection in hMEC cells align with well-
620 established prognostic markers in breast cancer associated with recurrence and poor clinical outcomes
621 (63, 66). Similarly, the frequent selection of chromosome 20 gain in hPDE cells mirrors the recurrent
622 amplification of this chromosome in pancreatic adenocarcinoma (62). These findings suggest that both
623 positive and negative selection cooperate to sculpt the tissue-specific aneuploidy landscapes
624 characteristic of different cancer types.

625 Our chromosomal instability screens also converge with recent work (72) in demonstrating tissue-specific
626 selection of chromosome 8q gain in mammary epithelial cells, with our quantitative fitness measurements

627 (s = 0.0133 in hMEC, s = 0.0624 in hMEL) supporting the proposed MYC-driven proliferative advantage.
628 However, unlike this prior study, we did not observe positive selection for chromosome 1q gain; in fact,
629 +1q showed negative selection in our bulk competition assays. This divergence likely reflects
630 fundamental differences in competitive dynamics between clonal isolation (72) and mixed-population
631 selection (this study). Additionally, the 21 population doublings in our screen may be insufficient for the
632 Notch poising phenotype to overcome the initial fitness costs of aneuploidy, whereas the 35-40 PD
633 timeframe and pre-established aneuploid backgrounds in the Watson et al. study may allow stress-
634 mitigation effects to emerge. This suggests that +1q provides a selective advantage specifically in
635 competitive scenarios where +1q-bearing cells remain rare within a population—a condition more likely
636 to occur in spatially structured tissues or during clonal evolution from single transformed cells than in bulk
637 culture competition.

638 A striking observation from our study is the asymmetry between chromosomal gains and losses: while in
639 vitro gain frequencies at Day 28 correlated significantly with TCGA tumor profiles, no such association
640 was observed for losses. This suggests that the selective pressures driving chromosomal losses in
641 tumors differ fundamentally from those acting on gains. We propose two non-mutually exclusive
642 explanations for this discordance. First, chromosomal losses may impose stronger deleterious effects on
643 cell viability in vitro, requiring additional oncogenic events—such as TP53 inactivation or whole-genome
644 doubling—to be tolerated during two-dimensional culture. Second, chromosomal losses may be selected
645 primarily by in vivo-specific pressures such as immune evasion, metabolic reprogramming, or metastatic
646 capacity, rather than by the proliferative advantage that drives gains in standard culture conditions (76).
647 Consistent with this interpretation, recent studies have documented the accumulation of cells harboring
648 specific chromosomal losses—including 10q, 16q, and 22q—in normal aging tissues such as the
649 mammary gland (70, 75). Notably, these loss events were not observed in our in vitro screens or in other
650 long-term two-dimensional evolution experiments (72), suggesting they are tolerated within three-
651 dimensional tissue architecture but do not confer proliferative advantages under standard culture

652 conditions. Supporting the importance of tissue context, gastric epithelial cells cultured as three-
653 dimensional organoids (with TP53 inactivation) frequently acquired 3p loss, a hallmark alteration in
654 gastric cancer (78). Together, these observations suggest that the tissue microenvironment—including
655 stromal interactions, immune surveillance, and spatial constraints—plays a critical role in determining
656 which aneuploidies are ultimately selected during tumor evolution in vivo.

657 # Methods

658

659 ***Cell Culture***

660 All cells were grown at 37°C with 5% CO2 levels. All cell media was supplemented with 1X pen-strep,
661 and 1X L-glutamine. hTERT human retinal pigment epithelial cells (RPE-1; ATCC CRL-4000) and SW48
662 cells (ATCC CCL-231) were incubated in DMEM, supplemented with 10% FBS. LoVo cells (ATCC CCL-
663 229) were incubated in Ham's F12-K media with 10% FBS. LS513 cells (ATCC CRL-2134) and hTERT
664 human pancreatic nestin-expressing cells (hPNEs; ATCC CRL-4023) were incubated in RPMI media with
665 10% FBS. CL11 cells (Cellosaurus CVCL_1978) were incubated in DMEM:F12 and 20% FBS. hTERT
666 p53-/- human colonic epithelial cells (hCECs; Ly et al.(36)) were cultured in a 4:1 mix of DMEM:Medium
667 199, supplemented with 2% FBS, 5 ng/mL EGF, 1 µg/mL hydrocortisone, 10 µg/mL insulin, 2 µg/mL
668 transferrin, 5 nM sodium selenite, pen-strep, and L-glutamine. hTERT human mammary epithelial cells
669 (hMEC) (67) were incubated in Mammary Epithelial Cell Growth Medium (MEGM, Lonza) supplemented
670 with 1% FBS and the MEGM SingleQuots kit (Lonza). hTERT human pancreatic duct epithelial cells
671 (hPDE; Cellosaurus CVCL_4376) were cultured with Gibco keratinocyte serum-free medium with 10%
672 FBS, 25 mg of bovine pituitary extract, and 2.5 µg of human recombinant EGF. Human melanocytes
673 (hMEL) with hTERT overexpression and p16/CDKN2A knocked out (gRNA:
674 CCCAACGCACCGAATAGTTACGG) were obtained from Richard Marais lab (University of Manchester)
675 were cultured with Melanocyte Growth Medium (MGM, Cell Applications) supplemented with 1% FBS.
676 For long-term storage, cells were cryopreserved at −80°C in 70% cell medium, 20% FBS, and 10%
677 DMSO. All cell lines were tested for mycoplasma.

678

679 ***Custom Tapestri Panel Design***

680 Panel Version 1 (CO261) comprises 330 probes across the 22 human autosomes and the X
681 chromosome. To identify candidate target regions for the panel, we used the Common SNP files

682 downloaded from UCSC(37,38) (snp151Common, hg19), and considered only synonymous variant
683 SNPs with a major allele frequency at >0.5 and <0.6. For cytobands with more than 4 synonymous
684 variants, we split the cytoband into 4 subregions based on the percentile of the cytoband coordinates (0-
685 25th percentile, 25-50th percentile, 50-75th percentile, and 75-100th percentile). From each subregion,
686 we randomly selected 1 SNP as a representative candidate. In cases where there were less than 5
687 synonymous variant SNPs, all SNPs were used. We submitted all candidate SNPs to the Tapestri Panel
688 Designer to generate a panel design and ensured that the designed probes targeted the candidate SNPs
689 and had similar GC contents. Next, randomly selected probes such that each chromosome had a probe
690 density of ~1 per 10MB. Panel Version 2 (CO610) comprises 352 probes across all 24 human
691 chromosomes. This panel was generated using Panel v1 as a base: first, we removed 61 probes that
692 had low PCR amplification efficiency based on total read counts per probe. Then we added 82 probes
693 such that each chromosome was targeted by at least 12 probes and included 4 probes targeting chrY.
694 To enable detection of lentiviral-delivered gRNAs, we added one probe targeting the region of the
695 construct containing the gRNA sequence and one probe targeting a region upstream as a vector control.
696 Similarly, for detection of lentiviral-delivered DNA barcodes, we added one probe targeting the region of
697 the construct surrounding the barcode sequence, and one probe targeting a region downstream as a
698 vector control. Support for the custom panel design and synthesis of the panel was provided by Mission
699 Bio (San Francisco, CA, USA). Panel maps were created using the karyoploteR R package(39).
700

701 ***Tapestri Single Cell DNA Sequencing***

702 Cell lines were trypsinized for 2-3 minutes, washed in room temperature Mg^{2+}/Ca^{2+}-free DPBS,
703 centrifuged at 300g for 5 minutes, and resuspended in DPBS at a concentration of 3K cells/uL. For the
704 experiment using the RPE1, SW48, LS513, LoVo, and CL11 cell lines, 600K cells from each cell line
705 were combined, centrifuged at 300g for 5 minutes, and resuspended in Tapestri Cell Buffer at a
706 concentration of 3.5K cells/uL. For the experiment using the RPE1, hPNE, and hCEC cell lines, 45K cells
707 from each cell line were combined, centrifuged at 300 x g for 5 minutes, and resuspended in Tapestri

708 Cell Buffer at a concentration of 4K cells/uL. For the KaryoCreate experiment, ~100K cells from each
709 condition were combined, centrifuged at 300 x g for 5 minutes, and resuspended in Tapestri Cell Buffer
710 at a concentration of 3.4K cells/uL. For the Aneuploidy induction experiment, ~200K cells from each
711 condition were combined, centrifuged at 300 x g for 5 minutes and resuspended in Tapestri Cell Buffer
712 at a concentration of 5K cell/ul. Cell droplet encapsulation, barcoding, and sequencing library preparation
713 were performed using the Tapestri instrument according to the manufacturer's instructions (Mission Bio,
714 San Francisco, CA, USA). Sequencing was performed using an Illumina NovaSeq 6000 or NextSeq 500
715 in 2x150bp paired-end format. After sequencing, deconvolution of barcodes, read counting, and variant
716 calling were handled by the online Tapestri Pipeline (v2.0.2)(25). The pipeline outputs both read counts
717 per probe for each cell and variant allele frequencies for called variants for each cell.
718
719 ***Low Pass Whole Genome Sequencing & Karyotyping***
720 Genomic DNA was extracted from cell pellets using 0.3 µg/µL Proteinase K (QIAGEN #19131) in 10mM
721 Tris pH 8.0 for 1 hour at 55°C, following heat inactivation at 70°C for 10 minutes. DNA was digested using
722 NEBNext dsDNA Fragmentase (NEB #M0348S) for 25 minutes at 37°C followed by magnetic DNA bead
723 cleanup with 2X Sera-Mag Select Beads (Cytiva #29343045). Library prep was performed using
724 NEBNext Ultra II DNA Library Prep Kit for Illumina (NEB #E7103) according to the manufacturer's
725 instructions, generating DNA libraries with an average library size of 320 bp. Quantification was
726 performed using a Qubit 2.0 fluorometer (Invitrogen #Q32866) and the Qubit dsDNA HS kit (Invitrogen
727 #Q32854). Libraries were sequenced on an Illumina NextSeq 500 at a target depth of 4-8 million reads.
728 Reads were trimmed using trimmomatic(40), aligned to the hg38 genome using bwa-mem(41), and
729 analyzed for copy number variants using the CopywriteR(42) R package. G-banded karyotyping of 100
730 RPE-1 cells was performed by WiCell Research Institute, Inc. (Madison, WI).
731

732 ***Cloning of sgRNAs***

733 We modified the scaffold sequence of pLentiGuide-Puro (Addgene #52963) by Gibson assembly to
734 contain the A-U flip (F) and hairpin extension (E) described by Chen et al(43). for improved sgRNA-dCas9
735 assembly, obtaining pLentiGuide-Puro-FE. sgRNAs were designed and cloned into this pLentiGuide-
736 Puro-FE vector according to the Zhang Lab General Cloning Protocol(44). To be suitable for cloning into
737 *BbsI*-digested vectors, sense oligos were designed with a CACC 5' overhang and antisense oligos were
738 designed with an AAAC 5' overhang. The sense and antisense oligos were annealed, phosphorylated,
739 and ligated into *BbsI*-digested pLentiGuide-Puro-FE for KaryoCreate purposes. Sequences were
740 confirmed by Sanger sequencing.

741

742 ***Gateway Recombination Cloning for Generation of Barcode Library***

743 pHAGE-CMV-DEST-PGKpuro-C-BC was a library of lentiviral vectors containing 24-bp random barcodes
744 that was built as described in Sack & Davoli et al., 2018(45). Destination vector pHAGE-CMV-DEST-
745 PGKpuro-C-BC and entry vector pDONR223_BFP (Addgene: 25891) are recombined following the
746 manufacturer's protocol. Briefly, 50 ng of entry vector and 100 ng of destination vector are mixed with LR
747 Clonase™ enzyme and incubated overnight at room temperature. The next day, the reaction mixture is
748 incubated with Proteinase K at 37°C for 10 minutes, followed by inactivation at 75°C for 15 minutes. The
749 reaction is then transformed into stbl3 bacterial competent cells, plated onto LB agar plates, and
750 incubated overnight at 37°C. Individual clones are collected into 96 well plates and expanded. Plasmid
751 is extracted from the bacterial culture using a 96-well mini-prep kit (Zymo kit, Zyppy 96 plasmid kit). All
752 clones were sequenced by Sanger sequencing at the site of the barcode using primer
753 ACTTGTGTAGCGCCAAGTGC. Duplicates were eliminated, and unique barcodes were retained in the
754 final library. BFP expression and Puromycin selection were validated by transfecting randomly selected
755 clones into HEK293T cells.

756

757 ***Lentivirus Production and Nucleofection***

758 For transduction of cells, lentivirus was generated as follows: 1 million 293T cells were seeded in a 6-
759 well plate 24 hours before transfection. The cells were transfected with a mixture of gene transfer plasmid
760 (2 µg) and packaging plasmids including 0.6 µg ENV (VSV-G; addgene #8454), 1 µg Packaging
761 (pMDLg/pRRE; addgene #12251), and 0.5 µg pRSV-REV (addgene #12253) along with $CaCl_2$ and 2×
762 HBS or using Lipofectamine 3000 (Thermo #L3000075).The medium was changed 6 hours later and
763 virus was collected 48 hours after transfection by filtering the medium through a 0.45-µm filter. Polybrene
764 (1:1000) was added to the filtered medium before infection.

765

766 ***KaryoCreate Experiments***

767 KaryoCreate experiments were performed as described in Bosco et al., 2023(14). Briefly, p53-/- hCEC
768 were first lentivirally transduced with pHAGE-KNL1Mut-dCas9 and selected with blasticidin. The cells
769 were then lentivirally transduced with the indicated sgRNAs and selected with puromycin. scDNA seq
770 was performed ~10 days after transduction with the gRNAs. The sequences of the gRNAs targeting the
771 centromeres of specific chromosomes are listed in Table S4 and were designed as described in Bosco
772 et al., 2023(14). To compare conditions, Fisher's exact test was performed in R using the `fisher.test()`
773 function, comparing the proportion of cells for each chromosome and sample that are diploid (copy
774 number = 2) and aneuploid (copy number = {1, 3, or 4} between the sgNC control and sample and the
775 given experiment sample. The Benjamini-Hochberg correction for multiple comparisons was applied to
776 p-values using `p.adjust()`.

777

778 ***Single Cell Aneuploidy Induction Screens and Selection Score Calculation***

779 Human immortalized cell lines (hPDE, hMEC, hMEL) were lentivirally transduced with the demultiplexing
780 barcode plasmids, as specified in Supplementary Table 5, and further selected with puromycin. A total of
781 1e+07 cells were treated with 1.5 µl of DMSO (control) or reversine (75nM or 150nM) for 36 to 48 hours.
782 After reversine treatment, cells were split and allowed to recover, with medium changes every 2-3 days.

783 Cells were passaged at 80-90% confluence using Gibco TrypLE Express Enzyme (1X). Cells were frozen
784 48 hours and 28 days after reversine release (Day 2 and Day 28, respectively) in freezing medium
785 containing 10% DMSO and 20% FBS in the respective growth medium.
786 To calculate the selection scores (https://github.com/fabio-alfieri/copy-number-annotation) for each arm,
787 a 2×2 contingency table was constructed, comparing the frequency of gain (or loss) events between two
788 experimental conditions (e.g., Day 2 vs. Day 28 at 150 nM Reversine). Fisher's exact tests were then
789 applied separately for gains and losses to assess whether the frequency of each alteration significantly
790 changed between time points. P-values were adjusted for multiple testing using the Benjamini–Hochberg
791 procedure. To quantify the direction and magnitude of selection, we computed selection scores as the
792 logarithm of Fisher's test odds ratios for gain and loss events, respectively. Positive scores indicate
793 selection for a specific copy-number alteration (gain or loss) over time, whereas negative scores denote
794 counter-selection.

795 **Calculation of Fitness Advantage from Aneuploidy Frequency Changes**

796 To estimate the selective advantage conferred by specific chromosomal aneuploidies during in vitro
797 culture, we calculated selection coefficients (s) from the change in aneuploidy frequency between Day 2
798 and Day 28 following reversine treatment. The selection coefficient represents the relative fitness
799 advantage per cell generation, where a fitness of (1 + s) indicates the proportional increase in
800 reproductive success compared to diploid cells.

801 We assumed a cell doubling time of 30 hours (1.25 days) based on growth curves for each cell line under
802 standard culture conditions. Over the 26-day interval between Day 2 and Day 28, cells underwent
803 approximately 20.8 cell divisions (26 days ÷ 1.25 days per division).

804 Under a model of constant selection, the frequency of an aneuploid population changes according to:

805 $$p_t / (1 - p_t) = (p_0 / (1 - p_0)) \times (1 + s)^t$$

806 where p_0 is the initial frequency of the aneuploid population at Day 2, p_t is the frequency at Day 28, t is
807 the number of cell generations (20.8), and s is the selection coefficient.

808 For chromosome 8q gain in hMEC cells:

809 - Day 2 frequency (p_0): 16% (0.16)
810 - Day 28 frequency (p_t): 20% (0.20)
811 - Number of generations (t): 20.8

812 Solving for s: $s \approx 0.0133$ (1.33% per generation)

813 A selection coefficient of s = 0.0133 indicates that chr8q gain cells have approximately 1.33% higher
814 fitness per cell division compared to diploid cells under these culture conditions. Assuming that the fitness
815 increase is due to decrease in doubling time, this would correspond to a 29.7 hours doubling time
816 compared to 30.

817 For chromosome 8q gain in hMEL cells:

818 - Day 2 frequency (p_0): 9% (0.09)
819 - Day 28 frequency (p_t): 26% (0.26)
820 - Number of generations (t): 20.8

821 Solving for s: $s \approx 0.0624$ (6.24% per generation). In hMEL cells, the chr8q gain shows a substantially
822 stronger selective advantage (s= 0.0624 or 6.24% per generation) compared to hMEC cells. Assuming
823 that the fitness increase is due to decrease in doubling time, this would correspond to a 28.2 hours
824 doubling time compared to 30.

825

826 ***Parsing and Counting of Barcoded Reads***

827 To detect specific gRNA or DNA barcode sequences, we searched for the known sequences against the
828 cell-associated aligned reads (cells.bam file) generated from the Tapestri Pipeline. Search queries were

829 conducted vcountPattern() using the Biostrings R package(46), with tolerance for up to 2 base
830 mismatches. BAM files were manipulated using the Rsamtools R package(47).
831
832 ***Cell Line Demultiplexing and Identification***
833 To demultiplex cells from different cell lines in the initial scDNA-seq experiment, we use the allele
834 frequency (AF) of variants that are called by GATC as part of the Tapestri Pipeline. Variants were filtered
835 by selecting those with standard deviations of AF >20 to select variants whose allele frequencies vary
836 the most across all cell lines. PCA was used to reduce the dimensions of the remaining variants. The top
837 4 principal components were embedded in two dimensions by UMAP and then clustered using the dbscan
838 method. The 5 clusters with the greatest number of cells were kept, corresponding to the 5 expected cell
839 lines. The remaining clusters, likely representing cell doublets, were discarded from further analyses.
840 This method was repeated for subsequent Tapestri experiments, adjusting for the expected number of
841 cell populations.
842 The cluster containing RPE1 cells in each experiment was identified by clustering with published deep
843 WGS of RPE1. Published RPE1 WGS data was obtained from SRA Accession ERR7477340(28,48).
844 Reads were aligned to the hg19 genome using bwa. MarkDuplicatesSpark and HaplotypeCaller from
845 GATK were used to mark duplicate reads and get AFs from called variants(49). The vcfR R package(50)
846 was used to extract the AFs for called variants common to the published data and our dataset. The mean
847 AF for each variant was calculated for each of the 5 cell lines. PCA was used to cluster our mean AF
848 dataset with the RPE1 AFs. The cell line that clustered most closely with the published RPE1 data was
849 labeled as RPE1 cells.
850
851 ***Copy Number Calling***
852 Copy number scores for each probe in each cell (cell-probe scores) were calculated relative to RPE1,
853 for which we know the copy number of each chromosome. The raw count matrix was normalized using
854 two alternative approaches: (A) by scaling each cell's mean to 1 (Equation 1) and then each probe's

median to 1 (Equation 2), or (B) by scaling each cell to cell's total read count and then rescaling to a global median of 1 (Equation 3) and by correcting to the probe-specific variability where each probe was adjusted using a coefficient c_{probe} proportional to its dispersion across cells (Equation 4). The normalized counts were then scaled such that the value of the median normalized RPE1 counts for each probe was set to 2 for all probes except those targeting chr10q, which were set to 3 (Equation 5). The identities of the remaining 4 populations of cells were identified by comparing their overall copy number profile with matched bulk WGS data.

(1) $$RC_{intermediate} = \frac{RC_{cell,\,probe}}{mean(RC_{cell}) + 1}$$

(2) $$RC_{norm} = \frac{RC_{intermediate}}{median(RC_{intermediate,\,probe}) + 0.05}$$

(3) $$RC_{intermediate} = \frac{RC_{cell,\,probe}}{\sum_{probe} RC_{cell} \cdot median(RC_{cell,\,probe \neq 0})}$$

(4) $$RC_{norm} = \frac{RC_{intermediate} + sd(RC_{intermediate,\,probe}) / 2}{median(RC_{intermediate,\,probe})}$$

(5) $$CN_{cell,\,probe} = \frac{CN_{WGS,\,probe} \cdot RC_{norm}}{median(RC_{norm,\,RPE1})}$$

Smooth copy number scores for each chromosome in each cell (cell-chromosome scores) were generated by taking the median of the probe-specific copy number values for probes targeting a common chromosome (Equation 6). This was also modified to calculate cell-chromosome-arm scores for probes common to a chromosome arm

(6) $$CN_{smooth,cell,chr} = median(CN_{cell,probe})$$

For all probes on chromosome *chr*.

Integer copy number values for each cell-chromosome were classified using Gaussian mixture models (GMMs) with either five components representing possible copy number values of 1, 2, 3, 4, and 5, or three components representing copy number values 1, 2, and 3. To generate the GMMs, the normalized counts for each probe for the RPE1 cells were fitted to Weibull distributions using the fitdistrplus R package(51). These Weibull parameters represented parameters for copy number = 2 for all probes except those targeting chr10q, which has 3 copies in RPE1. The scale parameters were then scaled for possible copy number values 1 through 6, relative to the RPE1 copy number: probes with RPE1 copy number = 2 were scaled by 50%, 100%, 150%, 200%, 250%, and 300% for copy number = 1, 2, 3, 4, 5 and 6; probes with RPE1 copy number = 3 were scaled by 33%, 67%, 100%, 133%, 167%, and 200% for copy number = 1, 2, 3, 4, 5 and 6. 500 Weibull-distributed values are drawn using each of the six parameter sets for each probe to simulate six matrices of 500 simulated cells. For each cell, the values were smoothed across the probes belonging to each chromosome to simulate cell-chromosome copy number values. The distribution of the scores for each chromosome was then fit to Gaussian (normal) distributions, separately for each copy number level. The result is a set of normal parameters (mean μ and standard deviation σ) for each chromosome for each value of copy number k = {1, 2, 3, 4, 5, 6}. The six copy number Gaussian components for each chromosome were combined into a GMM, representing the probability densities for each copy number value for that chromosome (Equation 7). Using Bayes rule and assuming equal priors, the posterior probability of a cell-chromosome copy number score being generated under each component k is given by Equation 8.

(7) $pdf\left(x = CN_{smooth,cell,chr}\right) = \frac{1}{\sigma\sqrt{2\pi}} \cdot e^{-\frac{1}{2}\left(\frac{x-\mu}{\sigma}\right)^2}$

(8) $P(k|x) = {pdf_k(x)}\Big/{\sum_{k=1}^{6} pdf_k(x)}$

903 Decision boundaries for the GMMs are calculated by finding the transitions between components, i.e.,
904 the point x where the probability density functions (PDFs) of the components are equal. We evaluated
905 copy numbers using GMMs including copy number components 1-5 throughout the study and 1-3 where
906 indicated. Upper boundaries for component 5 were calculated using components 1-6. Theoretical
907 sensitivity for each copy number component was calculated as the proportion of the component PDF that
908 falls within its decision boundaries (i.e., true positive rate). 5-fold cross validation was performed by
909 partitioning RPE1 cells into 5 equally sized groups and using each group once to evaluate a model
910 generated using the remaining 4 groups. R scripts for copy number calling were compiled into an R
911 package, karyotapR. karyotapR version 0.1 was used for analyses in this study.
912
913 ***Panel Simulations***
914 For the probe downsampling simulation of chromosome 2, 50 samples each of *n* probes from the set of
915 24 probes targeting chr2 were generated where *n* = {4, 6, 8 … 20, 22}. Copy numbers were called for
916 each set of probes for each cell. The sensitivity of the copy number calls was recalculated for the RPE1
917 cells as well as the theoretical sensitivity for all GMM components. This analysis was repeated for the set
918 of probes targeting chr6 where *n* = {4, 6, 8 … 14, 16}.
919 For the simulation of an expanded custom panel, the set of 120 probes targeting chromosomes 1, 2, 3,
920 4, 5, and 6 were sampled 50 times to produce 50 sets of the 120 probes in unique orders. Starting with
921 the first 4 probes of each set, copy numbers were called for RPE1 cells using those 4 probes, and again
922 as each additional probe was added to the set until all 120 probes were used for the calculation. This
923 procedure was repeated for each of the 50 sets. The sensitivity of copy number cells was recalculated
924 for the RPE1 cells at each step as well as the theoretical sensitivity for all GMM components using a
925 model with 5 components (with the upper boundary of the 5th component being calculated using a 6-
926 component model), and with 3 components where noted.
927 For the read depth simulation, the read count matrix was randomly downsampled to 80%, 60%, 40%,
928 and 20% of the total read counts using the downsampleMatrix function from the scuttle R package(52).

929 50 downsampled matrices were generated for each downsampling level. The sensitivity of copy number
930 cells was recalculated for the RPE1 cells at each step as well as the theoretical sensitivity for all GMM
931 components using a 5-component model. Least squares linear regression was performed at each copy
932 number level in R with the formula 'sensitivity ~ log(n.probes) + depth` where depth was a categorical
933 variable.
934
935 ***Comparison between KaryoTap and Arcwell***
936 We compared the copy number detection ability of KaryoTap with Arc-well, a scDNA-seq method of
937 similar throughput. Arc-well fastq files were aligned to the reference human genome hg38 using BWA-
938 mem (v0.7.17), and duplicates were removed using GATK (Genome Analysis Toolkit, v4.1.7.0) to
939 generate analysis-ready BAM files. To enable fair comparison with KaryoTap sequencing depth, Arc-
940 well data were downsampled to 30K and 15K reads per cell. The resulting BAM files were processed
941 using the R package CopywriteR (v1.18.0) to determine arm-level copy numbers. Downsampling to
942 15K reads resulted in qualitatively increased noisiness, with only 30-50% of full-depth copy number
943 events detected. For comparison, we downsampled KaryoTap RPE1 data to 40X depth (~15K reads
944 per cell). For cost comparison, we evaluated reagent costs based on current pricing. GenomePlex
945 WGA4, the DOP-PCR WGA product (60), costs $19.45–27.70 per cell, pricing a hypothetical 500-cell
946 experiment at $9,725 before sequencing costs. In contrast, KaryoTap costs approximately $0.50–1.00
947 per cell, representing less than 10% of the cost of alternative methods such as shallow scWGS based
948 on single-well cell capture, which costs approximately $8–10 per cell.
949
950

Figure and Table Legends

Figure 1

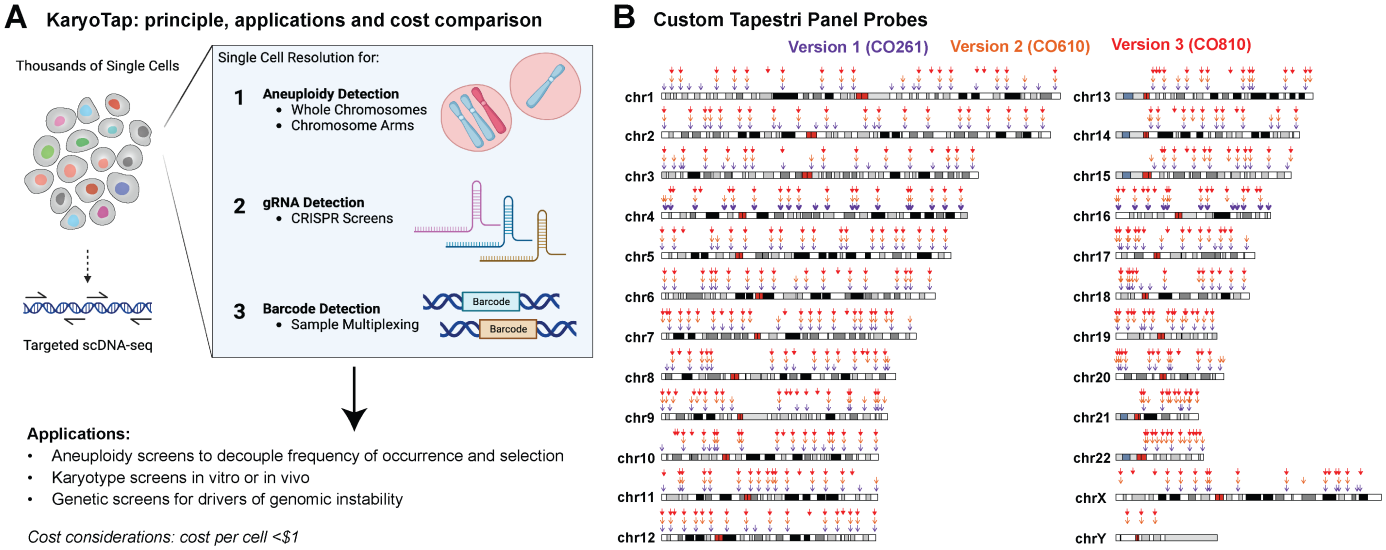

Figure 1

(A) Summary of KaryoTap as a novel single cell DNA sequencing method for high-throughput detection of aneuploidy in single cells in a cost efficient manner.
(B) Map of PCR probe locations (arrows) for custom Tapestri panels for KaryoTap Version 1 (CO261), Version 2 (CO610) and Version 3 (CO810) on human genome hg19. Red blocks indicate centromeres, grayscale blocks indicate the G-band intensity of cytobands, and blue blocks indicate acrocentric chromosome arms.

Figure 2

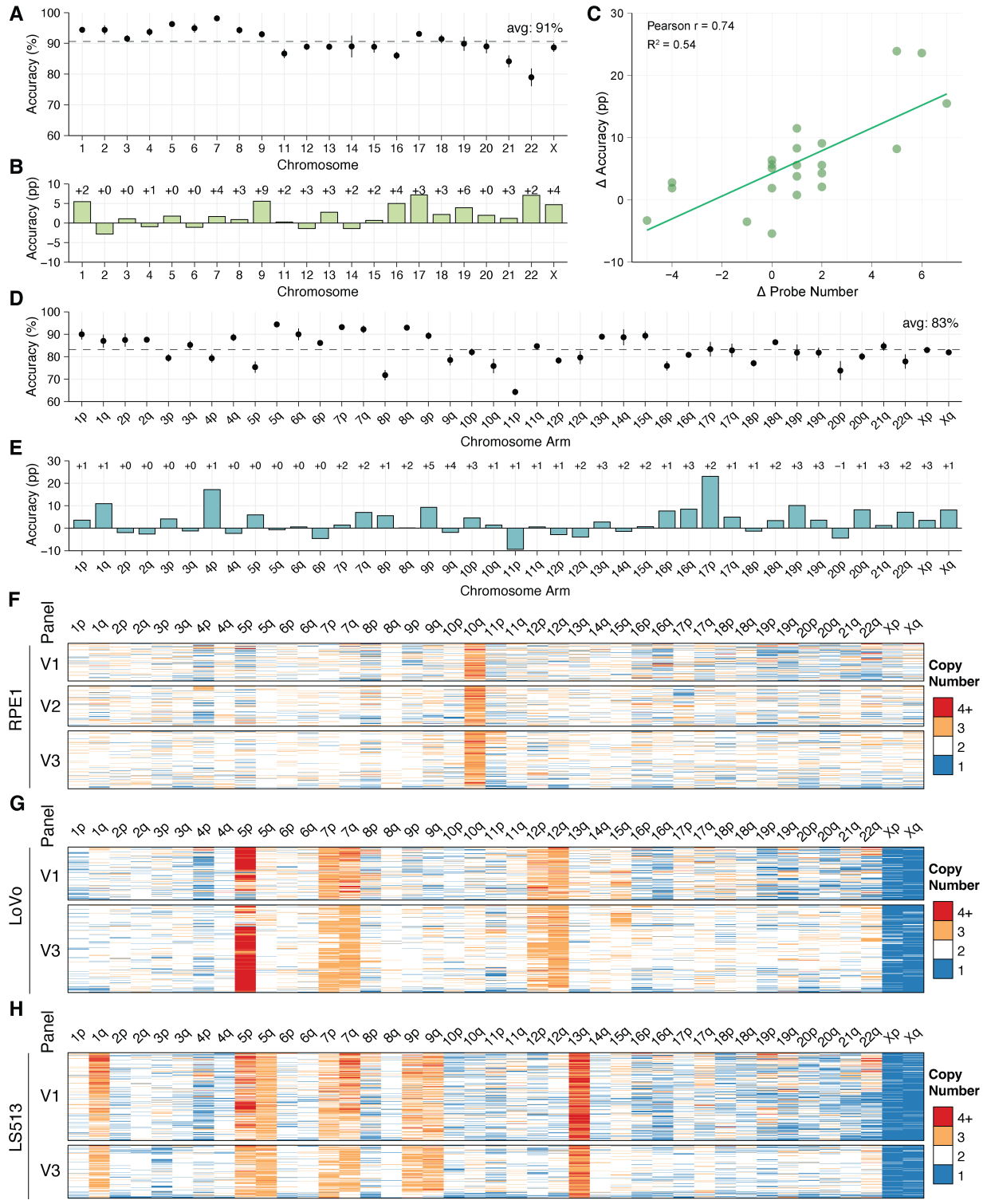

964

965 **Figure 2**

966 Copy number calling and lentiviral barcoding for custom KaryoTap panel Version 2.

967 **(A)** 5-fold cross validation of copy number call sensitivity for n=631 RPE1 cells by chromosome using
968 panel Version 3. Chr10 is omitted. Dot indicates mean accuracy and lines indicate ± mean absolute
969 deviation. Horizontal dotted line indicates average (avg) accuracy across chromosomes.
970 **(B)** Change in copy number call accuracy by chromosome for RPE1 cells between Version 3 and Version
971 2 panels. Δ Probe Number is the difference in number of probes targeting a given chromosome between
972 Version 3 and Version 2. pp: percentage points.
973 **(C)** Linear regression of the change in copy number call accuracy for RPE1 cells between Version 3 and
974 Version 2 panels on the change in probe number targeting each chromosome. **(D)** 5-fold cross validation
975 of copy number call accuracy for RPE1 cells by chromosome arms using custom Tapestri panel Version
976 3. Dot indicates mean accuracy and lines indicate ± mean absolute deviation. Horizontal dotted line
977 indicates average accuracy across chromosome arms. **(E)** Change in copy number call sensitivity by
978 chromosome arm for RPE1 cells between Version 3 and Version 2 panels.
979 **(F-H)** Heatmaps of GMM copy number calls for chromosome arms using panels Version 1, 2, and 3 for
980 cell lines RPE1, LoVo, and LS513.
981

982

983

Figure 3

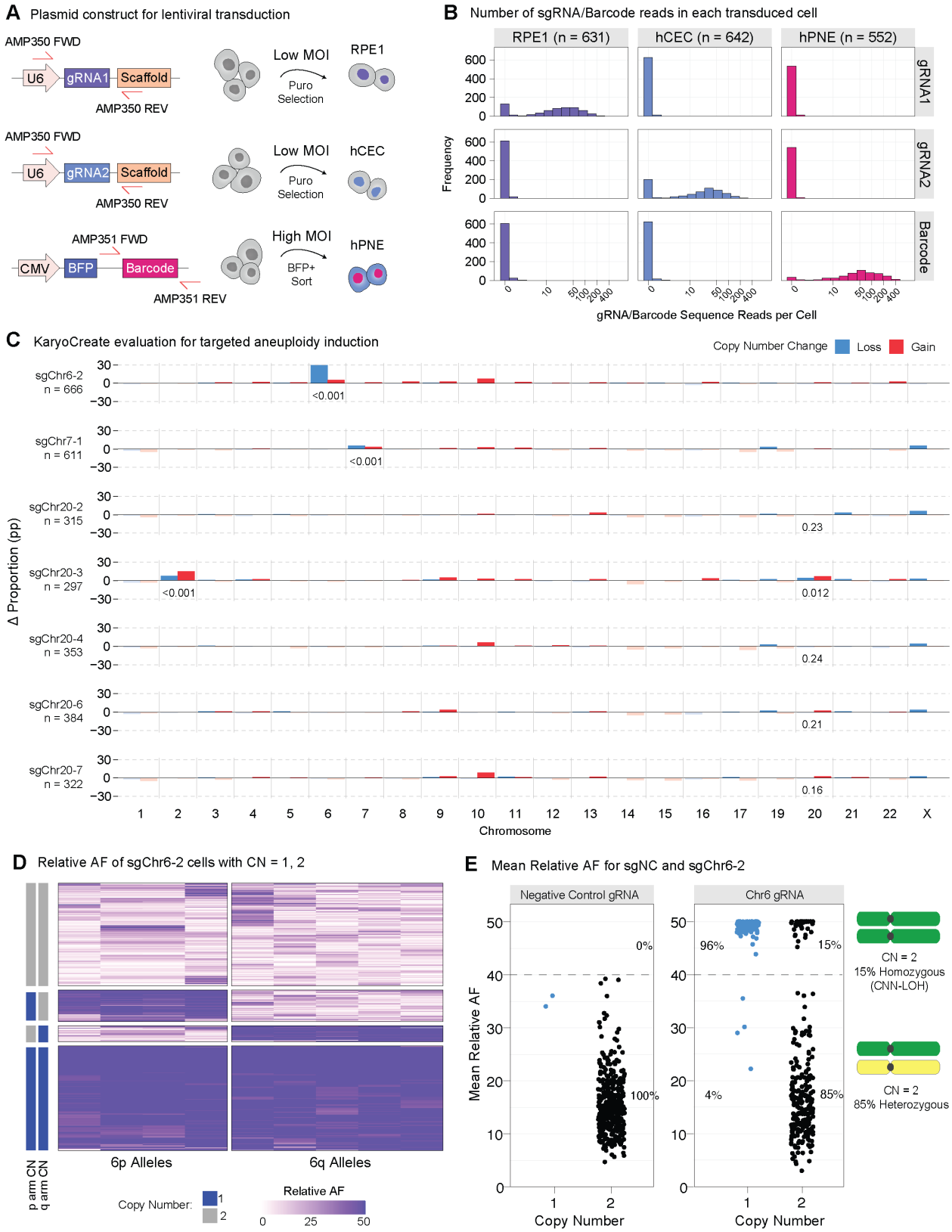
A Plasmid construct for lentiviral transduction
AMP350 FWD
U6
gRNA1
Scaffold
AMP350 REV
Low MOI
Puro Selection
RPE1
AMP350 FWD
U6
gRNA2
Scaffold
AMP350 REV
Low MOI
Puro Selection
hCEC
AMP351 FWD
CMV
BFP
Barcode
AMP351 REV
High MOI
BFP+ Sort
hPNE
B Number of sgRNA/Barcode reads in each transduced cell
RPE1 (n = 631)
hCEC (n = 642)
hPNE (n = 552)
gRNA1
gRNA2
Barcode
Frequency
gRNA/Barcode Sequence Reads per Cell
C KaryoCreate evaluation for targeted aneuploidy induction
Copy Number Change
Loss
Gain
sgChr6-2 n = 666
sgChr7-1 n = 611
sgChr20-2 n = 315
sgChr20-3 n = 297
sgChr20-4 n = 353
sgChr20-6 n = 384
sgChr20-7 n = 322
Δ Proportion (pp)
Chromosome
D Relative AF of sgChr6-2 cells with CN = 1, 2
6p Alleles
6q Alleles
p arm CN
q arm CN
Copy Number:
Relative AF
E Mean Relative AF for sgNC and sgChr6-2
Negative Control gRNA
Chr6 gRNA
Mean Relative AF
Copy Number
CN = 2
15% Homozygous (CNN-LOH)
CN = 2
85% Heterozygous

984

985 **Figure 3**
986 Evaluation of KaryoCreate and Loss of Heterozygosity.
987 **(A)** Plasmid constructs for lentiviral transduction of RPE1, hCEC D29, and hPNE cell lines. Probe pair
988 AMP350 amplifies a 253 bp region including a CRISPR gRNA sequence and part of the U6 promoter and
989 F+E scaffold. Probe pair AMP351 amplifies a 237 bp region including a barcode sequence.
990 **(B)** Number of reads in each cell that match the expected sequence of gRNA1, gRNA2, or barcodes in 3
991 transduced cell lines. X-axis is log-scaled. Number of cells in each cell line is indicated.
992 **(C)** Evaluation of KaryoCreate technology by KaryoTap panel Version 2. Bars represent the percentage
993 point (pp) change (Δ) in the proportion of chromosomal losses (1 copy) and gains (3+ copies), compared
994 to sgNC negative control (n = 398 cells). Chr18 was omitted due to additional copies of the chromosome
995 in the cell line. p-values from Fisher's Exact test comparing the proportion of cells with copy number = 2
996 to copy number = {1, 3, or 4} (i.e., diploid vs. aneuploid) in each chromosome in each sample to the
997 corresponding chromosome in the sgNC negative control sample are shown where $p < 0.1$. Additional p-
998 values > 0.1 are reported where relevant. All p-values are reported in Table S2. Bars with negative values
999 and $p > 0.1$ have reduced opacity for clarity.
1000 **(D)** Heatmap of relative VAFs for sgChr6-2 treated cells with 1 or 2 copies of chr6 as called by GMM, for
1001 9 originally heterozygous variants. Relative allele frequencies calculated as the absolute difference
1002 between raw allele frequency and 50%. 0 corresponds to balanced heterozygous alleles and 50
1003 corresponds to fully homozygous alleles. Heatmap rows split by k-means clustering where k=4 and sorted
1004 by hierarchical clustering. CN: copy number.
1005 **(E)** Mean relative VAFs for sgNC and sgChr6-2 treated cells with 1 or 2 copies of chr6 as called by GMM.
1006 0%-40% AF indicates heterozygous haplotype, 40%-50% AF indicates homozygous haplotype.
1007

1008

1009

Figure 4

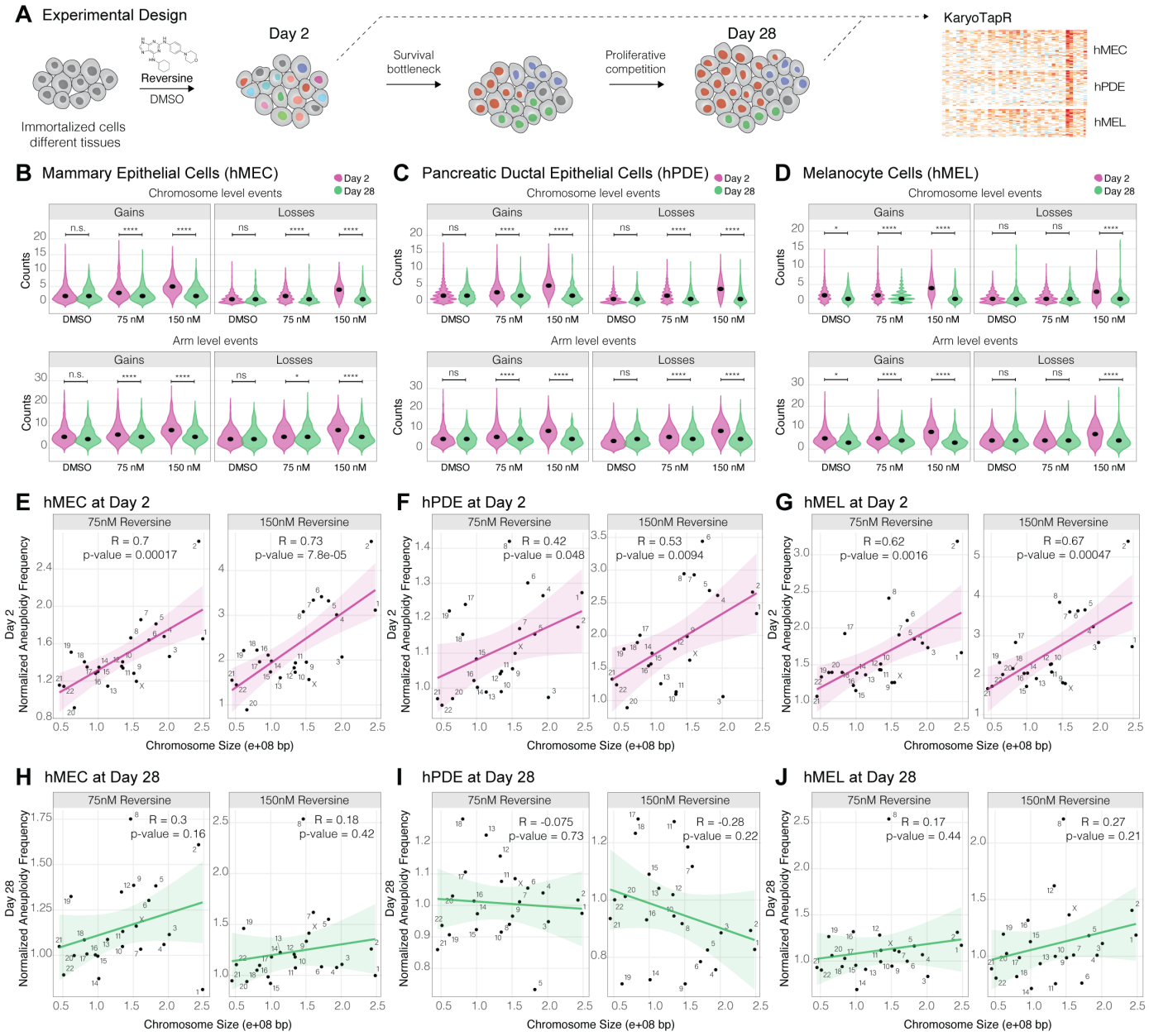

Figure 4

Reversine-Induced chromosomal instability and in vitro selection dynamics.

(A) Experimental design of reversine-induced chromosomal instability. Healthy cell lines (mammary epithelial cells, hMEC; pancreatic epithelial cells, hPDE; melanocyte cells, hMEL) were treated with either dimethyl sulfoxide (DMSO, vehicle control) or varying concentrations of reversine (75 nM and 150 nM). Cells were analyzed at Day 2 for immediate chromosomal instability and selection and monitored through Day 28 to evaluate survival bottlenecks and proliferative competition. Outcomes were measured using KaryoTapR to capture chromosome-level and arm-level gains and losses.

1020 **(B-D)** Chromosome-level and arm-level instability induced by reversine treatment in mammary epithelial
1021 cells (hMEC, B), pancreatic epithelial cells (hPDE, C), and melanocyte cells (hMEL, D) at Day 2 and Day
1022 28. Violin plots show the counts of chromosome and arm-level gains and losses across DMSO-treated
1023 and reversine-treated conditions (75 nM and 150 nM). Green represents Day 2, pink represents Day 28,
1024 indicating how chromosomal instability evolves. Statistical tests comparing condition groups are indicated
1025 (*$p < 0.05$, **$p < 0.01$, ****$p < 0.0001$; n.s.: not significant).
1026 **(E-J)** Correlation between chromosome size and aneuploidy frequency (gains and losses) following
1027 reversine treatment. Scatter plots display the normalized (reversine frequencies over DMSO control)
1028 aneuploidy frequency versus chromosome size for hMEC (E, H), hPDE (Panels F, I), and hMEL (G, J).
1029 E-G depict analyses at Day 2, and H-J illustrate Day 28. Regression lines represent trends for 75 nM and
1030 150 nM reversine treatments; correlation coefficients (Pearson's R) and p-values are provided for
1031 statistical significance.
1032
1033

1034

Figure 5

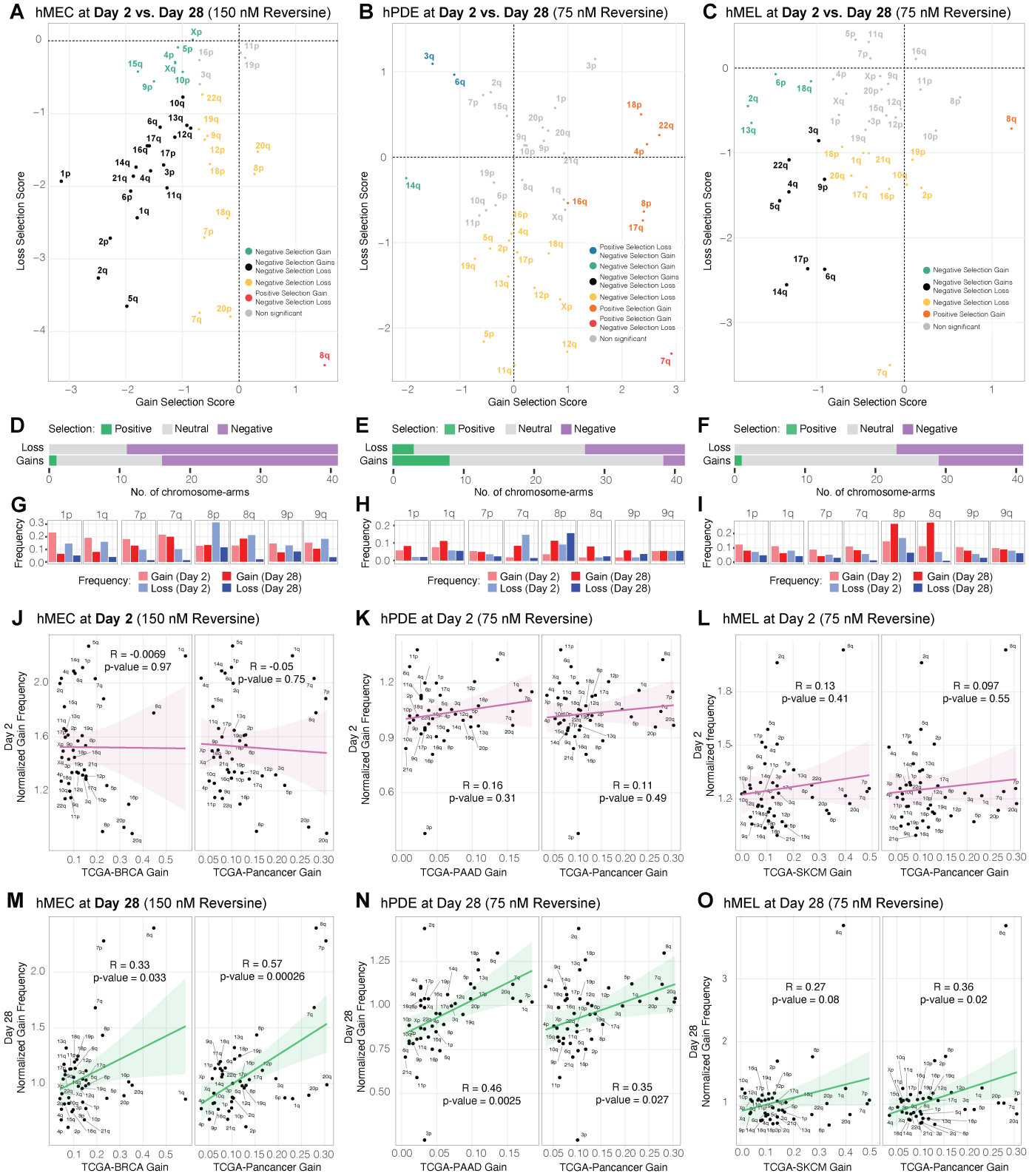

Figure 5

Quantification of selection forces and correlations between reversine-induced chromosomal alterations in cell lines and TCGA cancer data.
(A-C) Selection scores for chromosome gains and losses across experimental conditions. Scatter plots display gain selection scores (x-axis) versus loss selection scores (y-axis) for hMEC (G, 150 nM reversine), hPDE (H, 75 nM reversine), and hMEL (I, 75 nM reversine). Positive selection (colored dots) indicates chromosomes that are preferentially gained (red or yellow) or lost (blue or turquoise) over time. Negative selection indicates chromosomes that are under negative selective pressure. Non-significant changes are indicated in gray.
(D-F) Bar plot showing the number of chromosome arms under different types of selection (positive, neutral or negative) for arm gains and losses.
(G-I) Frequency of gains and losses across specific chromosomal arms (of chromosome 1, 7, 8, and 9), at the two time points, Day 2 and Day 28.
(J-O) Comparison of chromosome-arm gain frequencies induced by reversine with cancer amplification frequency from TCGA data. Panels compare normalized chromosome arm gain frequencies at Day 2 (A-C) and Day 28 (D-F) with TCGA amplifications from respective cancer types (hMEC with BRCA, hPDE with PAAD, and hMEL with SKCM) and TCGA-Pancancer. Scatter plots include correlation coefficients (Pearson's R) and p-values. Green and pink regression lines distinguish between gains at Day 2 (pink) and Day 28 (green).

1056 **Supplementary Data**

1057 **Systematic Evaluation of Technical Parameters Influencing Copy Number Classification**
1058 **Performance**

1059 To comprehensively characterize the factors governing copy number calling accuracy in KaryoTap, we
1060 conducted a series of systematic simulations using scDNA-seq data from RPE1 cells. These simulations
1061 examined three key technical parameters: probe number per chromosome, copy number classification
1062 scheme (5-component versus 3-component Gaussian mixture models), and sequencing depth. By
1063 independently varying each parameter while controlling for others, we aimed to quantify their relative
1064 contributions to classification sensitivity and guide optimization strategies for future panel designs.

1065 ***Probe Number Determines Classification Sensitivity***

1066 To confirm that copy number classification accuracy depends on the number of probes targeting a
1067 chromosome rather than the absolute size of the chromosome itself, we performed downsampling
1068 analysis on chromosomes 2 and 6. We randomly sampled n probes from the complete probe sets
1069 targeting chromosome 2 (24 total probes) and chromosome 6 (18 total probes), generating 50
1070 independent samples for each value of n. Copy number classification accuracy was recalculated for
1071 RPE1 cells using each downsampled probe set.

1072 The downsampling analysis revealed a clear relationship between probe number and classification
1073 performance. For chromosome 2, median accuracy decreased progressively from 95.8% with the full
1074 complement of 24 probes to 68.8% with only 4 probes. Similarly, chromosome 6 showed a decline from
1075 91.4% (18 probes) to 66.8% (4 probes), confirming that probe number, not chromosome size, is the
1076 primary determinant of classification accuracy (**Fig S5A**).

1077 Importantly, the variability of classification accuracy also increased markedly as probe number
1078 decreased. The interquartile range (IQR) of accuracy distributions expanded from 0.8 percentage points
1079 with 22 probes to 9.14 percentage points with 4 probes for chromosome 2, and from 1.5 percentage
1080 points with 16 probes to 11.6 percentage points with 4 probes for chromosome 6 (**Fig S5A**). This
1081 increasing variability indicates that sparse probe coverage not only reduces average accuracy but also
1082 introduces greater inconsistency in classification performance across independent samples.

1083 These patterns of decreasing accuracy and increasing variance with fewer probes were consistently
1084 observed across all five copy number levels (1-5 copies) when examining theoretical sensitivity calculated
1085 from the Gaussian mixture model components (**Fig S5B**). This consistency across copy number states
1086 demonstrates that the relationship between probe number and classification performance is a
1087 fundamental property of the method rather than an artifact specific to diploid chromosomes.

1088 ***Simulated Panel Expansion Defines Optimal Probe Requirements***

1089 Having established that increasing probe number enhances sensitivity, we sought to determine the
1090 optimal probe coverage required to achieve high classification accuracy across all copy number states.
1091 To address this question, we simulated progressively larger panels by combining all probes targeting
1092 chromosomes 1 through 6 (120 probes total) and treating them as measurements from a single

hypothetical chromosome. This approach is valid because all six chromosomes are diploid in RPE1 cells, allowing us to pool their probe measurements while maintaining a known ground truth of 2 copies.

For each of 50 simulation trials, we constructed panels by iteratively sampling the 120 probes without replacement, recalculating RPE1 copy number classification and theoretical sensitivity after adding each probe until all 120 probes were incorporated. This progressive addition strategy allowed us to observe how sensitivity evolves as panel size increases, revealing both the rate of improvement and potential saturation points.

Mean theoretical sensitivity increased monotonically with probe number across all copy number levels, though the rate of improvement and asymptotic behavior varied by copy number state (**Fig S5C**). For the 5-component classification model (distinguishing 1, 2, 3, 4, and 5 copies), the simulation demonstrated that achieving at least 90% mean sensitivity requires 4 probes for 1-copy states, 20 probes for 2-copy states, 50 probes for 3-copy states, and 90 probes for 4-copy states. The 5-copy state proved most challenging, reaching a maximum mean sensitivity of approximately 87% even with the full 120-probe panel. The variability in sensitivity estimates across the 50 trials decreased progressively as probe number increased, indicating that larger panels provide not only higher accuracy but also more consistent performance.

For applications where precise copy number enumeration is less critical than distinguishing between loss, neutral, and gain states, we evaluated a simplified 3-component Gaussian mixture model representing 1 copy (loss), 2 copies (neutral), and ≥3 copies (gain). Under this classification scheme, sensitivity improvements were more pronounced (**Fig S5D**). The 90% sensitivity threshold was achieved at 4 probes for loss states, 20 probes for neutral states, and 26 probes for gain states. Furthermore, 99% sensitivity—representing near-perfect classification—could be attained with 22 probes for loss detection, 66 probes for neutral state classification, and 76 probes for gain detection. These results demonstrate that the choice of classification granularity substantially impacts probe requirements, with simpler classification schemes achieving high accuracy with fewer probes.

Sequencing Depth Shows Minimal Impact on Classification Sensitivity

While probe number emerged as a critical determinant of classification performance, we also investigated whether sequencing depth—the average number of reads per cell per probe—significantly influences copy number calling accuracy. To evaluate this parameter, we systematically downsampled the read count matrix from our experimental dataset to 80%, 60%, 40%, and 20% of the original average depth (corresponding to approximately 68, 51, 34, and 17 reads per cell per probe, respectively, from the full depth of 85 reads). For each downsampling level, we generated 50 independent downsampled datasets and recalculated copy number classifications for RPE1 cells.

Across all copy number levels, the effect of reduced sequencing depth on theoretical sensitivity was modest: mean theoretical sensitivity decreased by an average of only 0.4 percentage points at 80% depth, 0.8 percentage points at 60% depth, 1.8 percentage points at 40% depth, and 4.4 percentage points at 20% depth relative to full sequencing depth. These marginal decreases indicate that, beyond a moderate threshold of approximately 35-50 reads per cell per probe, additional sequencing depth yields diminishing returns in terms of classification accuracy.

To formally test whether the effects of sequencing depth and probe number on sensitivity were independent or synergistic, we performed analysis of variance (ANOVA) on the combined simulation data. The lack of a significant interaction term (p = 0.9-1.0 for all copy number levels) confirmed that these two technical parameters influence classification performance through independent mechanisms. This independence has important practical implications: it suggests that optimizing probe number and sequencing depth can be approached as separate design considerations, with probe number being the primary lever for improving sensitivity and sequencing depth primarily affecting data quality and reliability rather than fundamental classification capability.

The minimal sensitivity gains beyond moderate sequencing depths also have favorable economic implications. Since sequencing costs scale directly with depth, these results indicate that cost-efficient experimental designs can achieve near-optimal classification performance without requiring excessive sequencing coverage. For most applications, targeting 40-60 reads per cell per probe should provide an optimal balance between classification accuracy and sequencing cost.

Summary and Design Recommendations

Our systematic simulation analyses establish probe number as the dominant determinant of copy number classification sensitivity in KaryoTap, with sequencing depth playing a secondary role beyond moderate coverage thresholds. The relationship between probe number and sensitivity follows a logarithmic pattern, with diminishing returns as probe density increases but meaningful improvements achievable through strategic probe addition, particularly for smaller chromosomes and chromosome arms that are underrepresented in genome-proportional designs.

The choice between 5-component and 3-component classification models substantially impacts probe requirements, with the simpler 3-component model achieving high sensitivity with considerably fewer probes. For applications focused on detecting aneuploidy (presence or absence of gains/losses) rather than precise copy number enumeration, the 3-component model represents an efficient approach that maintains high sensitivity while minimizing sequencing costs.

These findings provide quantitative guidelines for designing future KaryoTap panels tailored to specific experimental objectives, balancing classification sensitivity against practical constraints of panel size and sequencing budget. The independence of probe number and sequencing depth effects further allows these parameters to be optimized separately, facilitating flexible experimental designs appropriate for diverse research applications.

GMM-based Theoretical Accuracy (KaryoTap version V1)

The empirical accuracy for copy number calls in RPE1 only demonstrates the ability to detect 2 copies of a chromosome. We determined the theoretical accuracy for calling copy numbers of 1, 2, 3, 4, and 5 by calculating the proportion of each GMM component distribution that would be correctly classified. Overall, the highest theoretical accuracy was detected for 1 copy with an average of 97%, decreasing with each additional copy; 2 copies had an average sensitivity of 83% and 3 copies had 64% (**Fig S3E**). The theoretical sensitivity for 2 copies strongly correlated with the empirical accuracy for RPE1 calls (Pearson r = 0.97). As expected, theoretical sensitivity at all 5 copy number levels decreased for chromosomes

with fewer probes (**Fig S3E**). Theoretical arm-level sensitivity averaged 95% for 1 copy, 74% for 2 copies, and 53% for 3 copies.

Cost Comparison of KaryoTap compared to Similar Methods

To evaluate Karyotap compared to other single-cell genotyping methods, we compared KaryoTap to Arc-well data downsampled to 30K and 15K reads per cell. Downsampling to 15K reads showed qualitative increases in noisiness, with only 30-50% of full-depth events detected. In contrast, KaryoTap RPE1 data at comparable depth (~15K reads per cell) maintained robust detection. In terms of cost, GenomePlex WGA4 (DOP-PCR WGA (60) costs $19.45–27.70 per cell, pricing a 500-cell experiment at $9,725 before sequencing. Alternative shallow scWGS methods based on cell capture in single wells cost approximately $8-10 per cell (61). KaryoTap experiments cost approximately $0.5-1 per cell—less than 10% of these alternatives. By achieving comparable detection sensitivity at a fraction of the cost compared to WGS methods, KaryoTap provides a scalable and cost-effective solution for high-throughput aneuploidy detection that overcomes the size-dependent biases inherent to WGS-based approaches.

Supplementary Figure 1

A Whole-Genome sequencing

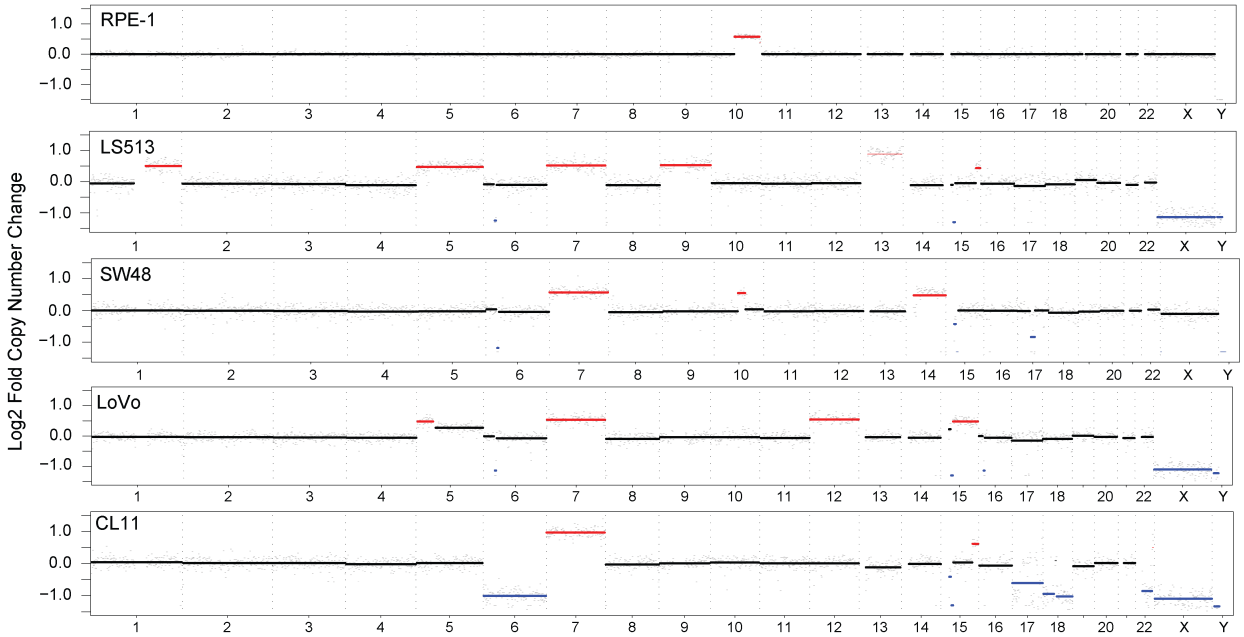

B RPE-1 Representative Karyotype

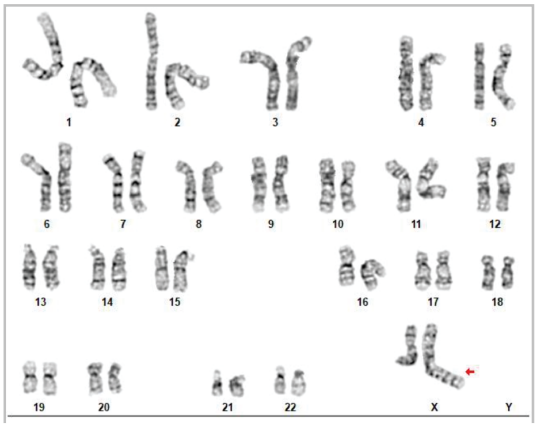

100/100: 3 copies 10q (translocated to X)

- 3/100: 3 copies 12
- 1/100: 3 copies 9, 3 copies 18
- 1/100: 3 copies 13

C UMAP

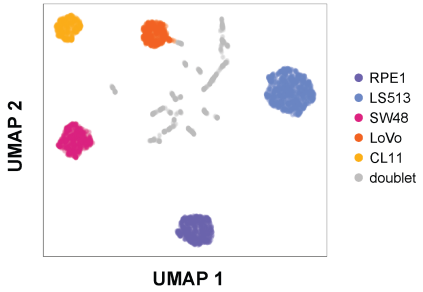

D PCA

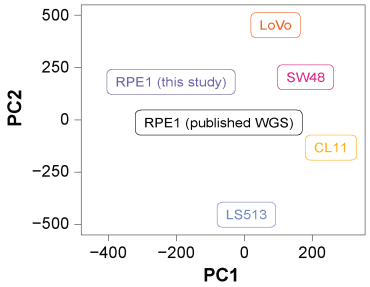

E Cell-probe Copy Number

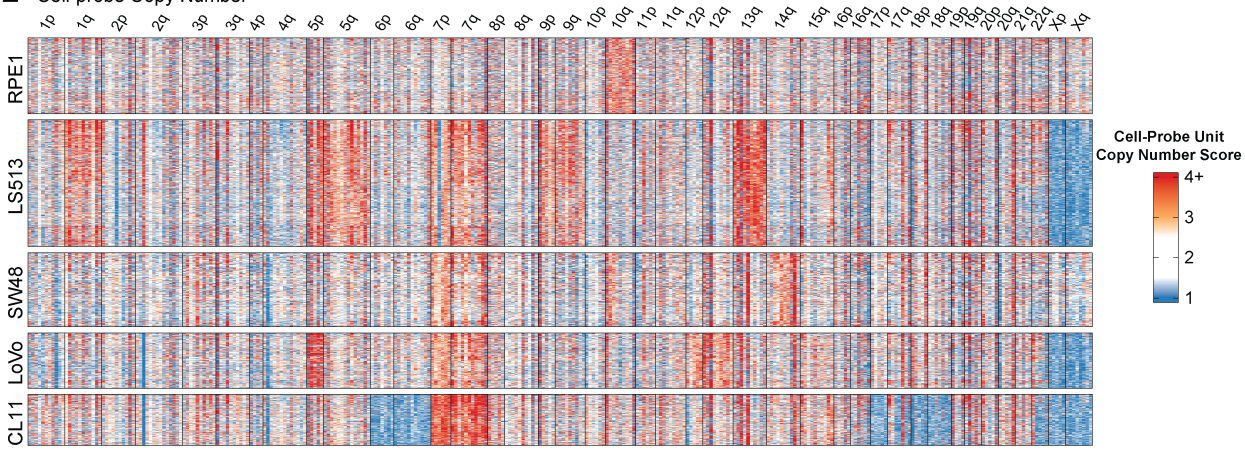

1188

1189 **Supplementary Figure 1**
1190 **(A)** Bulk low-pass whole genome sequencing of RPE1, LS513, SW48, LoVo, and CL11 cell lines. Red
1191 highlight indicates amplification of at least one copy of highlighted segment; blue similarly indicates
1192 deletion.
1193 **(B)** Representative g-banded karyogram of RPE1, indicating additional copy of chr10q translocated to
1194 the X chromosome (red arrow).
1195 **(C)** UMAP projection of top 4 principal components of allele frequencies for N=2,986 cells representing
1196 5 cell lines. Clustering was performed using the dbscan method. Cells were considered doublets if they
1197 were not members of the 5 largest clusters.
1198 **(D)** PCA plot of first two principal components of mean allele frequencies for previously published deep
1199 sequencing of RPE1 and the 5 cell lines analyzed by scDNA-seq.
1200 **(E)** Heatmap of cell-probe copy number values for five cell lines using custom Tapestri panel Version 1.
1201 Probes are organized by chromosome arm in genomic order.
1202

Supplementary Figure 2

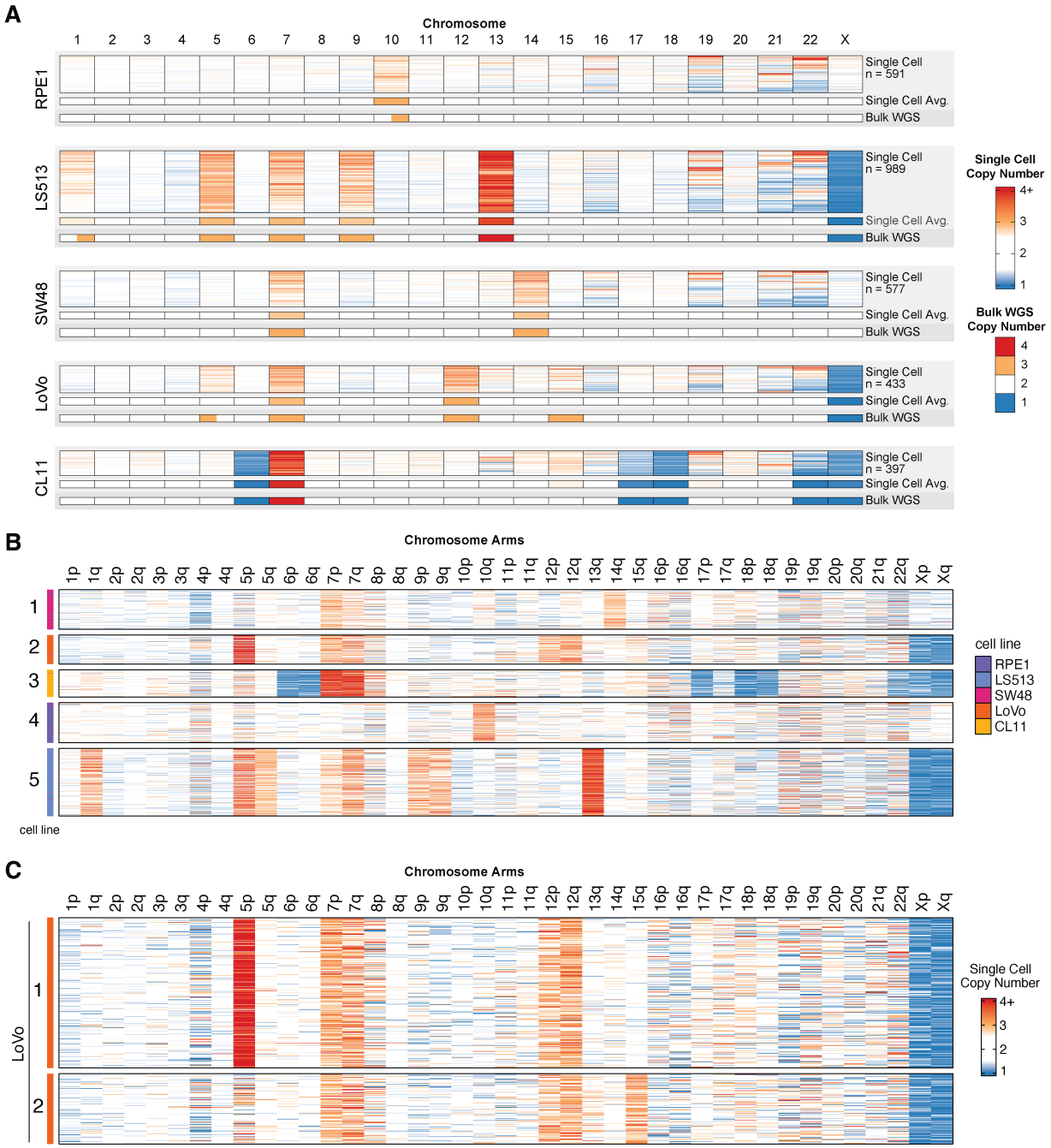

Supplementary Figure 2

(A) Heatmap of copy number scores for each cell-chromosome unit for 5 cell lines using custom Tapestri panel Version 1. Upper blocks indicate copy number scores for each cell, middle blocks indicate average intensity of upper blocks, and lower blocks indicate copy number from bulk WGS (see Fig S1A). Half-filled lower blocks indicate chromosome arm-level aneuploidy. Number of cells included in single-cell blocks is indicated.

(B) Heatmap of GMM calls for chromosome arms across 5 cell lines using v1 panel.

(C) Heatmap for further clustering within LoVo.

Supplementary Figure 3

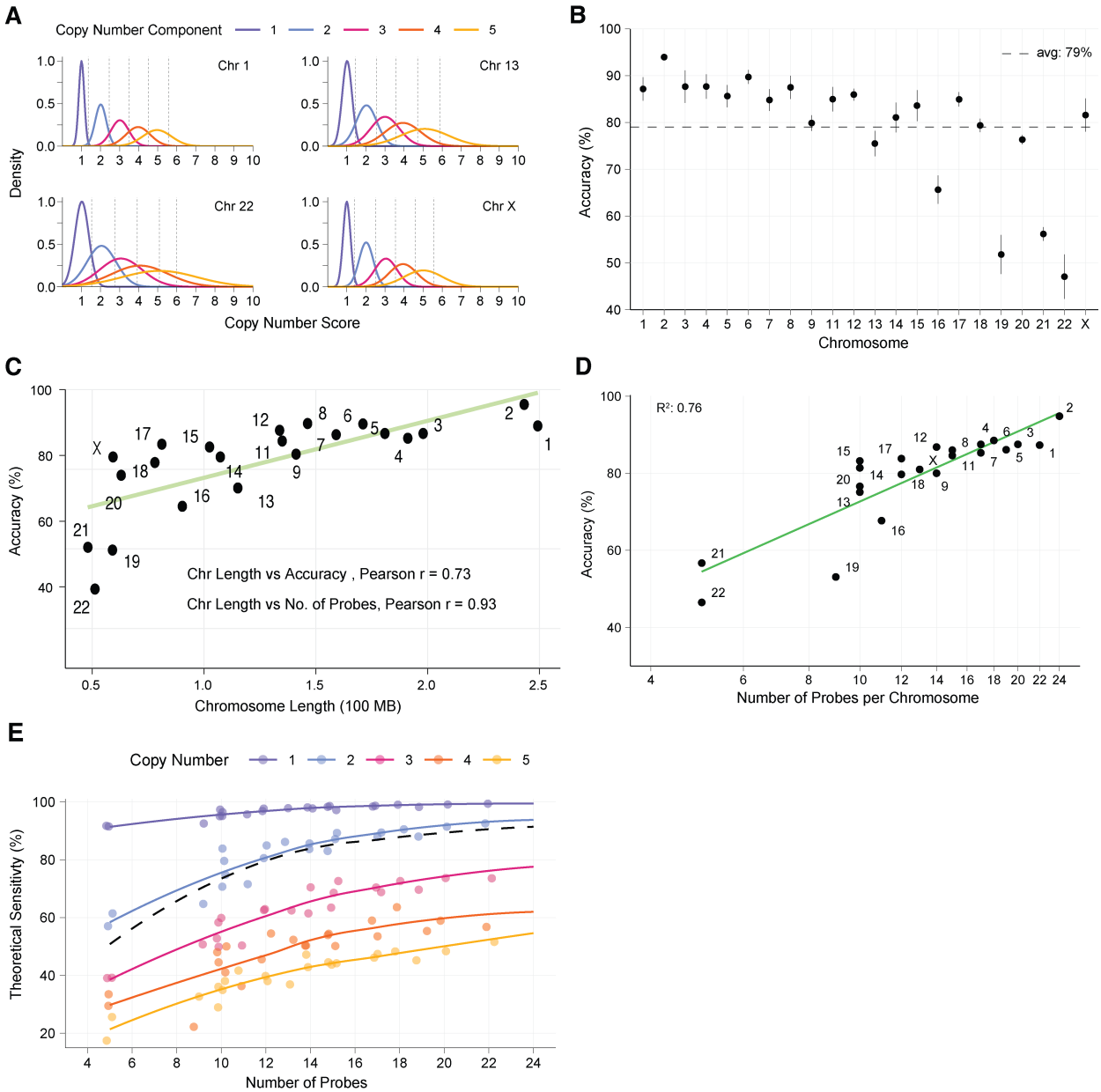

<u>Supplementary Figure 3</u>

(A) Probability density functions of Gaussian mixture models (GMM) fit for chromosomes 1, 13, 22, and X using RPE1 cells. Dotted lines indicate decision boundaries between GMM components.

(B) 5-fold cross validation of copy number call accuracy for RPE1 cells by chromosome. Chr10 is omitted. Dot indicates mean accuracy, and lines indicate ± mean absolute deviation. Horizontal dotted line indicates average (avg) accuracy across chromosomes.

(C) Chromosome length (in 100 megabases) vs. accuracy of RPE1 panel Version 1 copy number calls chromosome. Chr10 is omitted. Trendline fit by linear regression.

(D) Correlation between number of probes per chromosome and karyotap chromosome-copy-number call accuracy.

1224 **(E)** Theoretical copy number call sensitivity for each chromosome and copy number level calculated from
1225 GMMs. Points are slightly jittered horizontally to decrease overlapping.
1226

Supplementary Figure 4

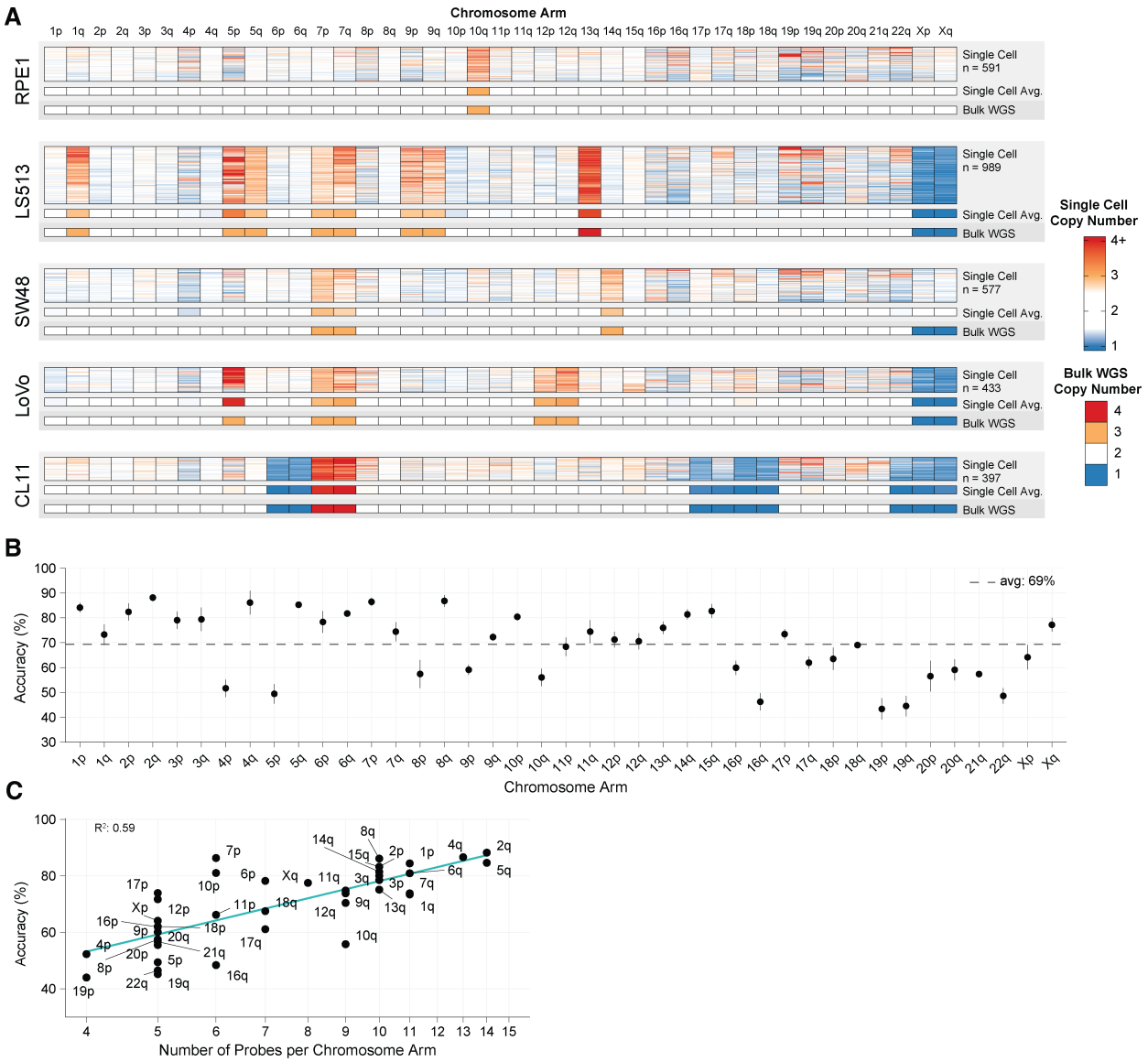

Supplementary Figure 4

(A) Heatmap of copy number scores for each cell, smoothed across chromosome arms, for five cell lines using custom Tapestri panel Version 1. Upper blocks indicate copy number scores for each cell; middle blocks indicate average intensity of upper blocks, and lower blocks indicate copy number from bulk WGS (see Fig S1A).

(B) 5-fold cross validation of copy number call accuracy for RPE1 cells by chromosome arm. Dot indicates mean accuracy and lines indicate ± mean absolute deviation. Horizontal dotted line indicates average accuracy across chromosome arms.

(C) Linear regression of RPE1 copy number call accuracy for each chromosome arm on number of probes per chromosome arm. X-axis is log-scaled to reflect log transformation of number of probes in regression.

Supplementary Figure 5

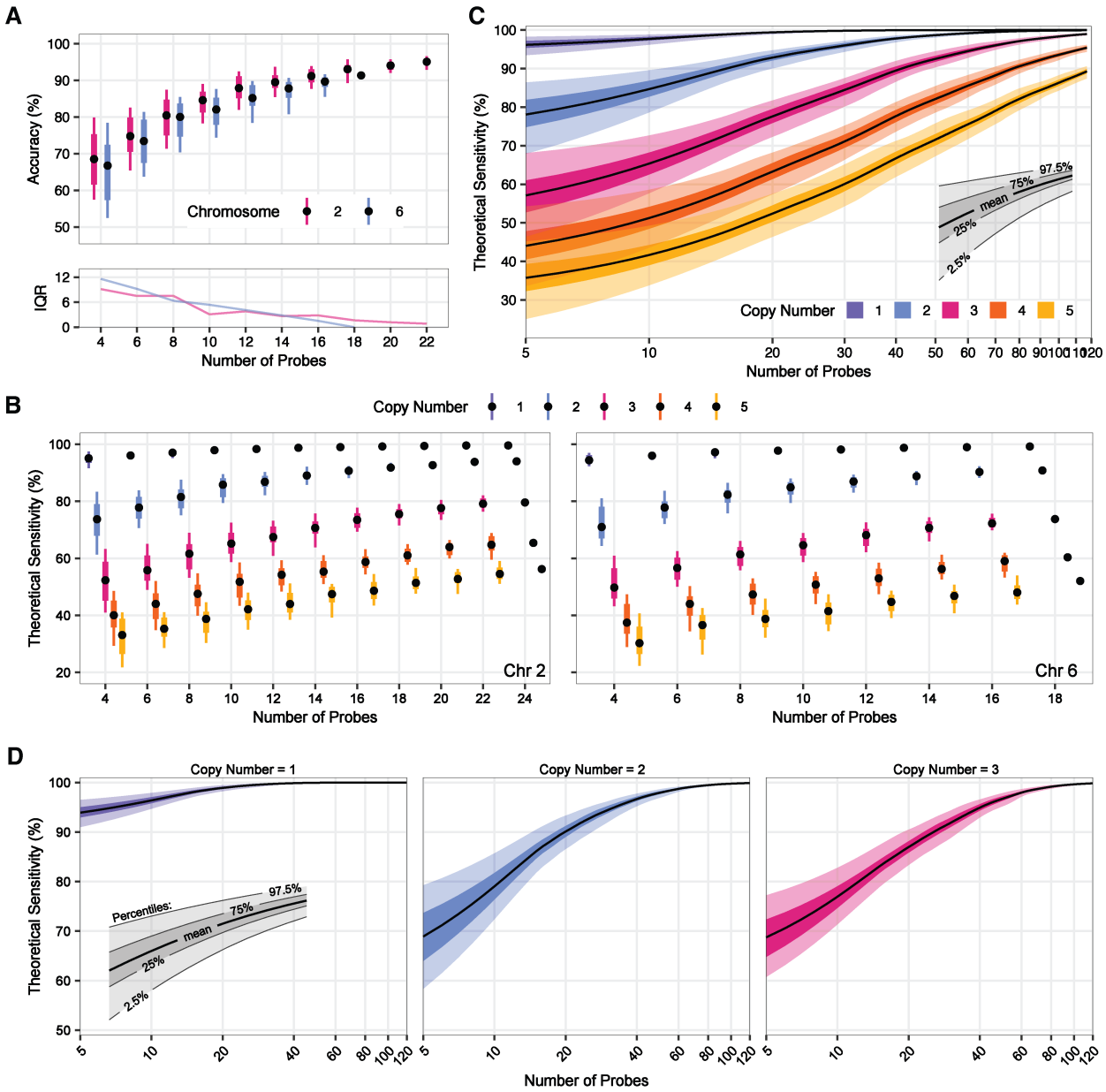

<u>Supplementary Figure 5</u>

Effects on copy number call accuracy on probe sampling simulations.
(A) Box plots and interquartile range (IQR) of accuracy from 50 probe downsampling simulations for chr2 and chr6.Boxes encompass middle 50%, whiskers encompass middle 95%, dot indicates median.
(B) Theoretical sensitivity of 50 panel simulations. Values for each copy number level were smoothed by Loess regression. The black line represents the mean, the darker inner shading indicates the middle 50% of the data, and the lighter outer shading represents the middle 95% of the data.
(C) Theoretical sensitivity of 50 panel simulations. Values for each copy number level were smoothed by Loess regression. The black line represents the mean, the darker inner shading indicates the middle 50% of the data, and the lighter outer shading represents the middle 95% of the data.

(D) Theoretical copy number call sensitivity of 50 panel simulations, using a 3 component GMM. Values for each copy number level were smoothed by Loess regression. The black line represents the mean, the darker inner shading indicates the middle 50% of the data, and the lighter outer shading represents the middle 95% of the data.

Supplementary Figure 6

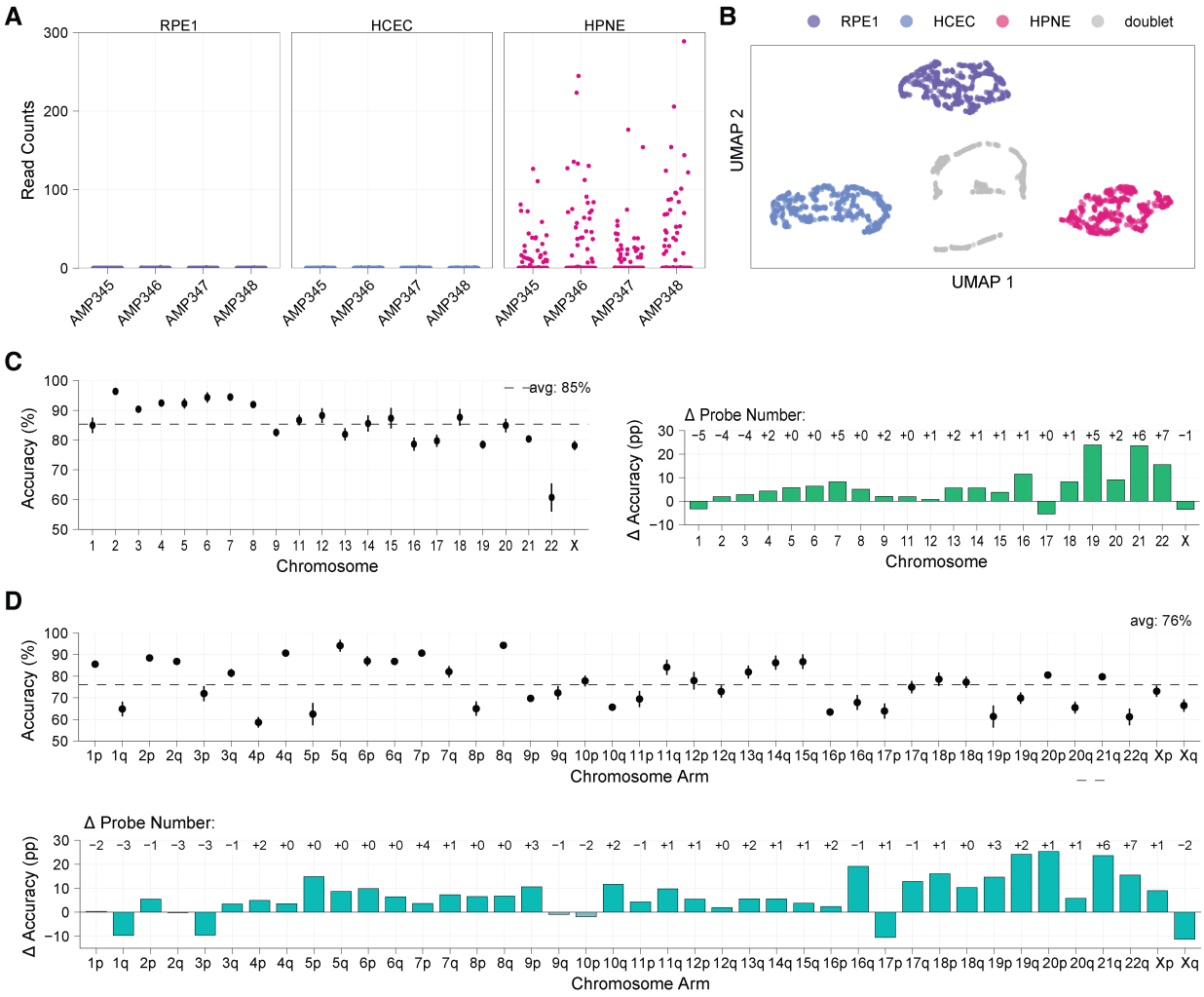

Supplementary Figure 6

(A) Read counts per cell of four probes targeting chrY across 3 cell lines.

(B) UMAP projection of top 2 principal components of allele frequencies for N=2,347 cells representing 3 cell lines. Clustering was performed using the dbscan method. Cells were considered doublets if they were not members of the 3 largest clusters.

(C) 5-fold cross validation of copy number call sensitivity for RPE1 cells by chromosome using panel Version 2. Chr10 is omitted. Dot indicates mean accuracy, and lines indicate ± mean absolute deviation. Horizontal dotted line indicates average (avg) accuracy across chromosomes. On the right, the barplot shows the change in copy number call accuracy by chromosome for RPE1 cells between Version 2 and Version 1 panels. Δ Probe Number is the difference in number of probes targeting a given chromosome between Version 2 and Version 1. pp: percentage points.

(D) 5-fold cross validation of copy number call accuracy for RPE1 cells by chromosome arms using custom Tapestri panel Version 2. Dot indicates mean accuracy, and lines indicate ± mean absolute deviation. Horizontal dotted line indicates average accuracy across chromosome arms. On the right, the barplot shows the change in copy number call accuracy by chromosome arm for RPE1 cells between

1274 Version 2 and Version 1 panels. Δ Probe Number is the difference in number of probes targeting a given
1275 chromosome arms between Version 2 and Version 1. pp: percentage points.
1276
1277
1278

Supplementary Figure 7

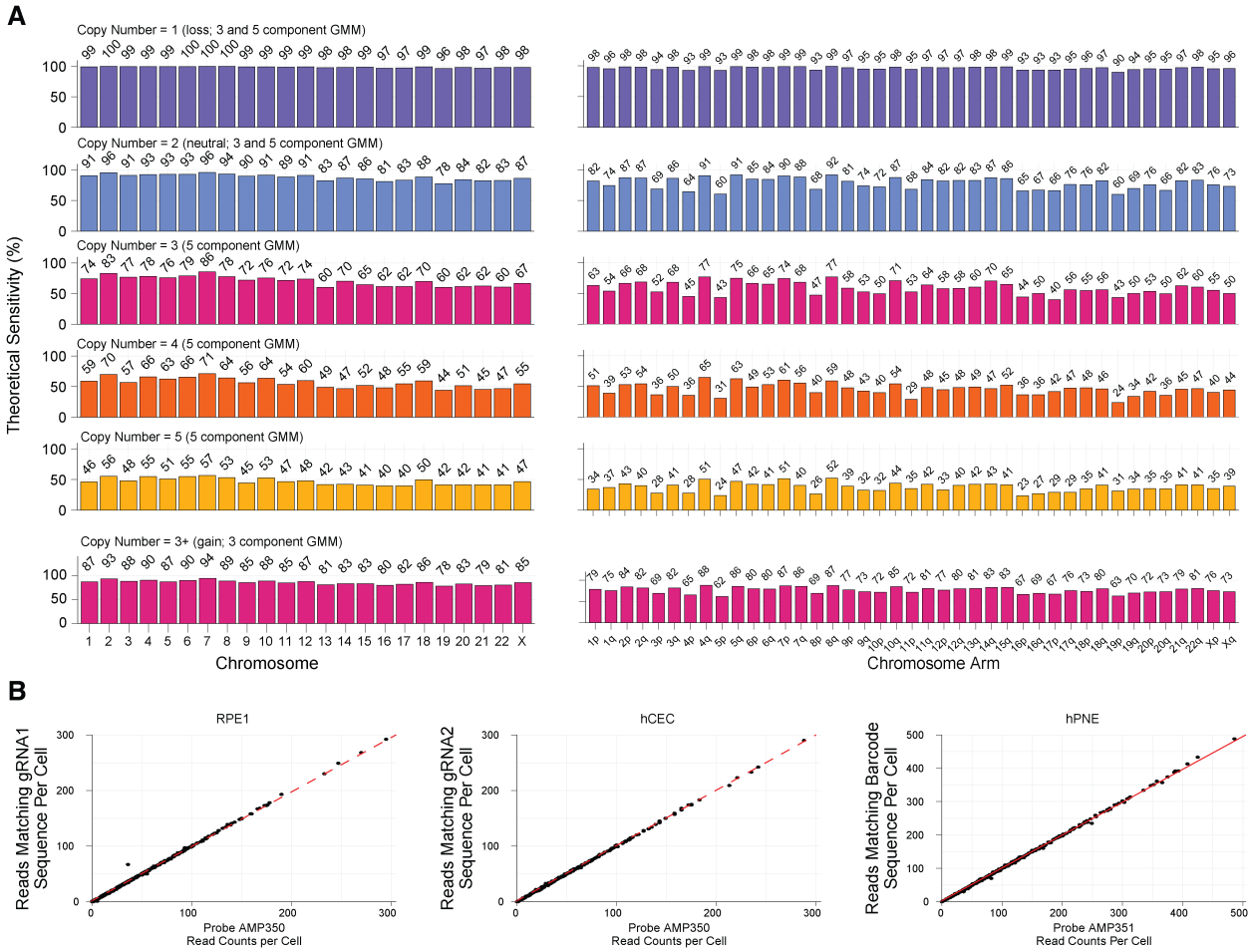

Supplementary Figure 7

(A) Mean theoretical accuracy of panel Version 3 copy number calls for each chromosome at copy number values of 1, 2, 3, 4 and 5.

(B) Relationship between read counts per cell for either the gRNA or DNA Barcode probes (x-axis) and the number of reads per cell that match the specific gRNA or DNA Barcode sequences (y-axis). Dotted red line indicates $x = y$.

Supplementary Figure 8

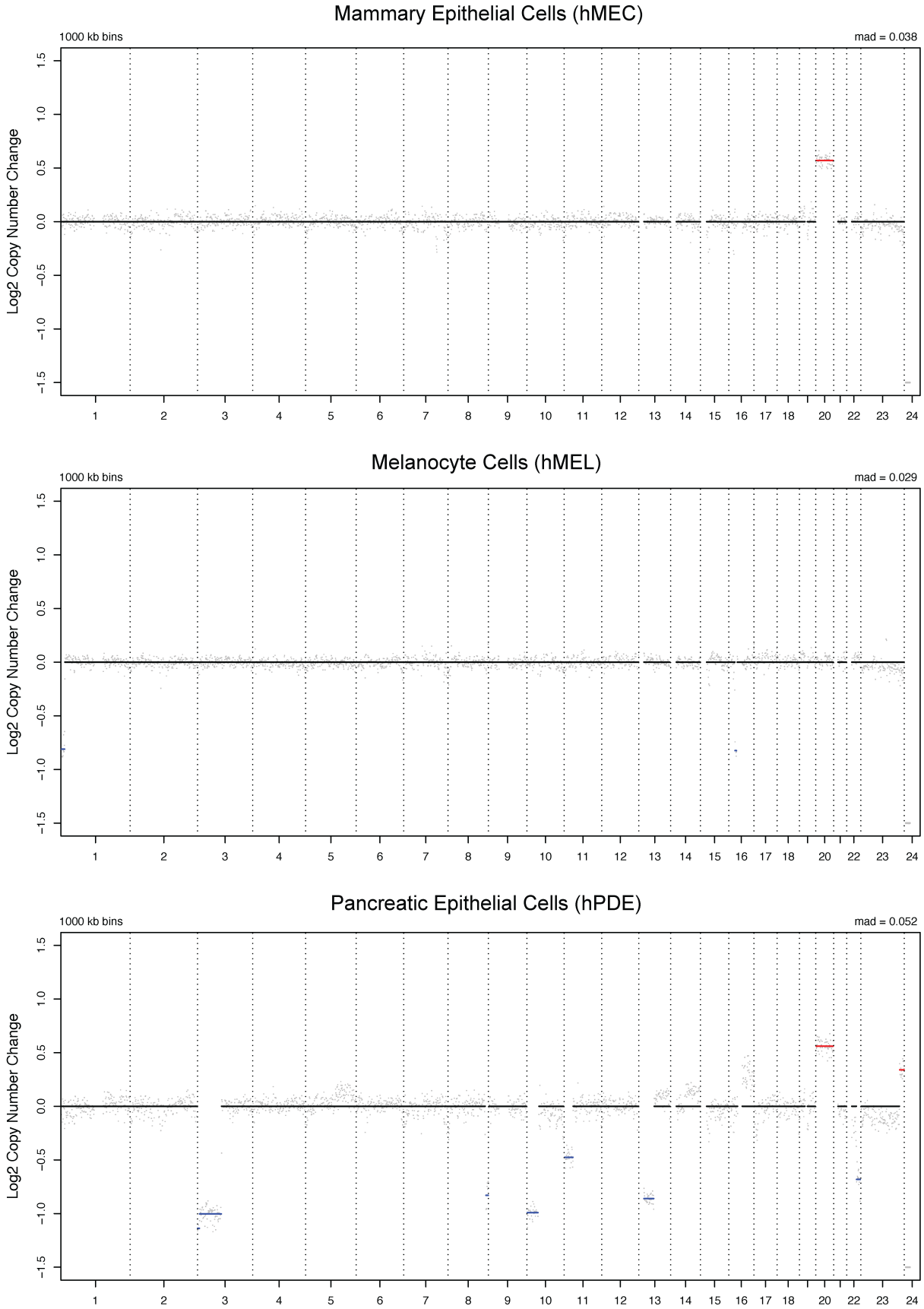

1289

1290 **Supplementary Figure 8**
1291 Low-pass WGS profile for mammary epithelial cells (hMEC), melanocyte cells (hMEL) and pancreatic
1292 epithelial cells (hPDE).
1293
1294
1295

Supplementary Figure 9

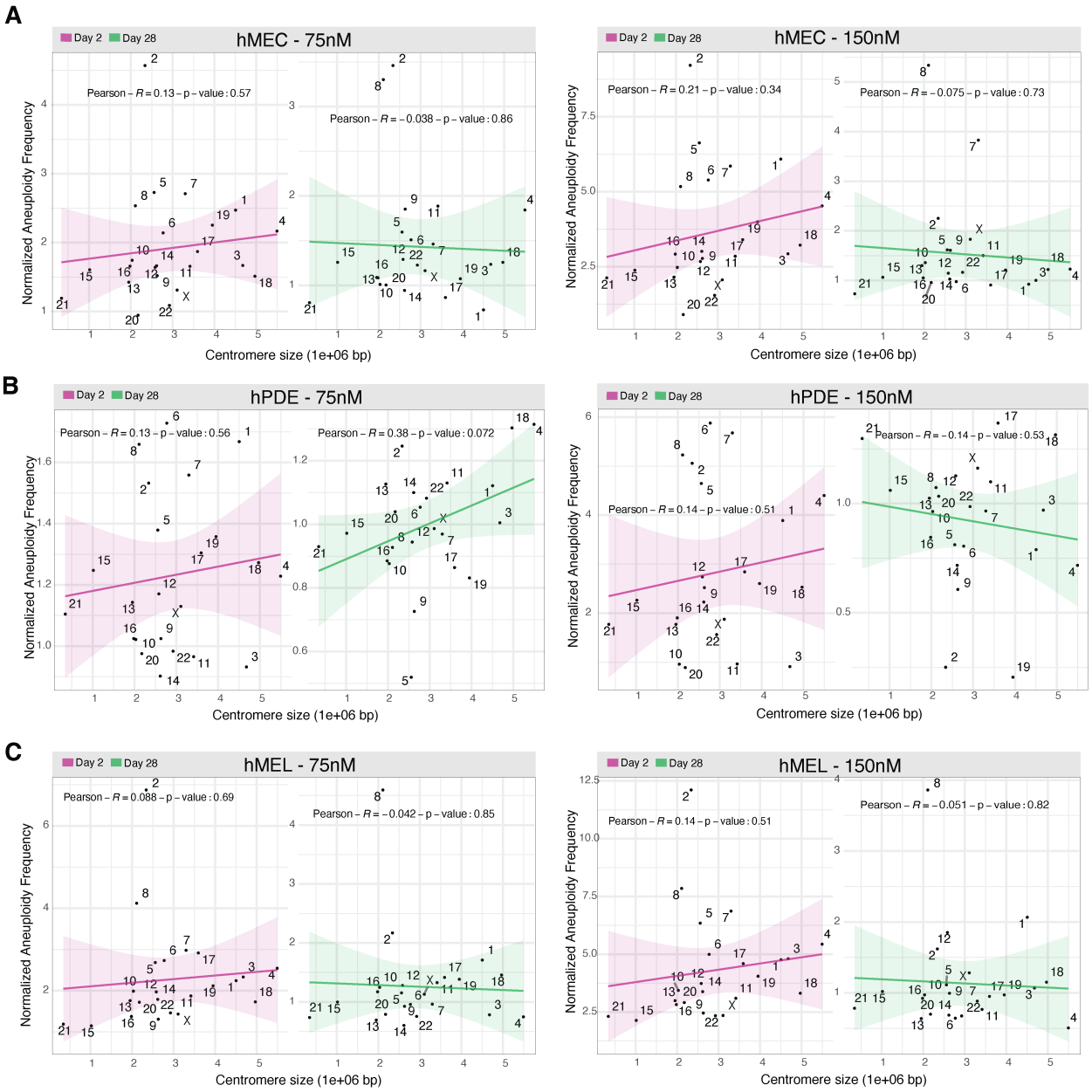

Supplementary Figure 9

Correlation between centromere size and aneuploidy frequency (gains and losses) following reversine treatment for **(A)** mammary epithelial cells (hMEC), **(B)** melanocyte cells (hMEL) and **(C)** pancreatic epithelial cells (hPDE). Regression lines represent trends for 75 nM and 150 nM reversine treatments; correlation coefficients (Pearson's R) and p-values are provided for statistical significance.

Supplementary Figure 10

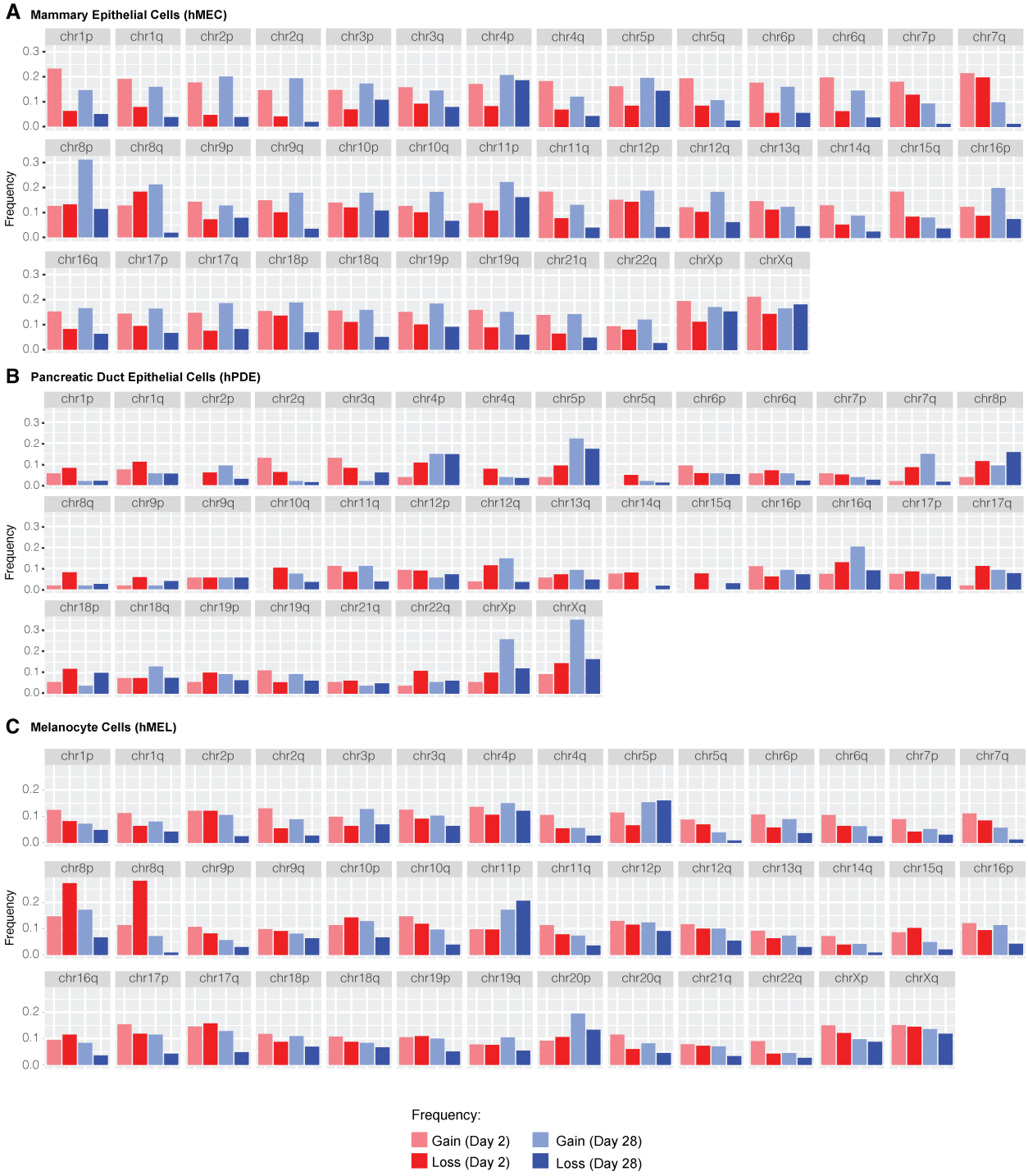

Supplementary Figure 10

Frequency of gains and losses across all chromosomal arms at the two time points, Day 2 and Day 28 for hMEC **(A)**, hPDE **(B)**, and hMEL **(C)**.

Supplementary Figure 11

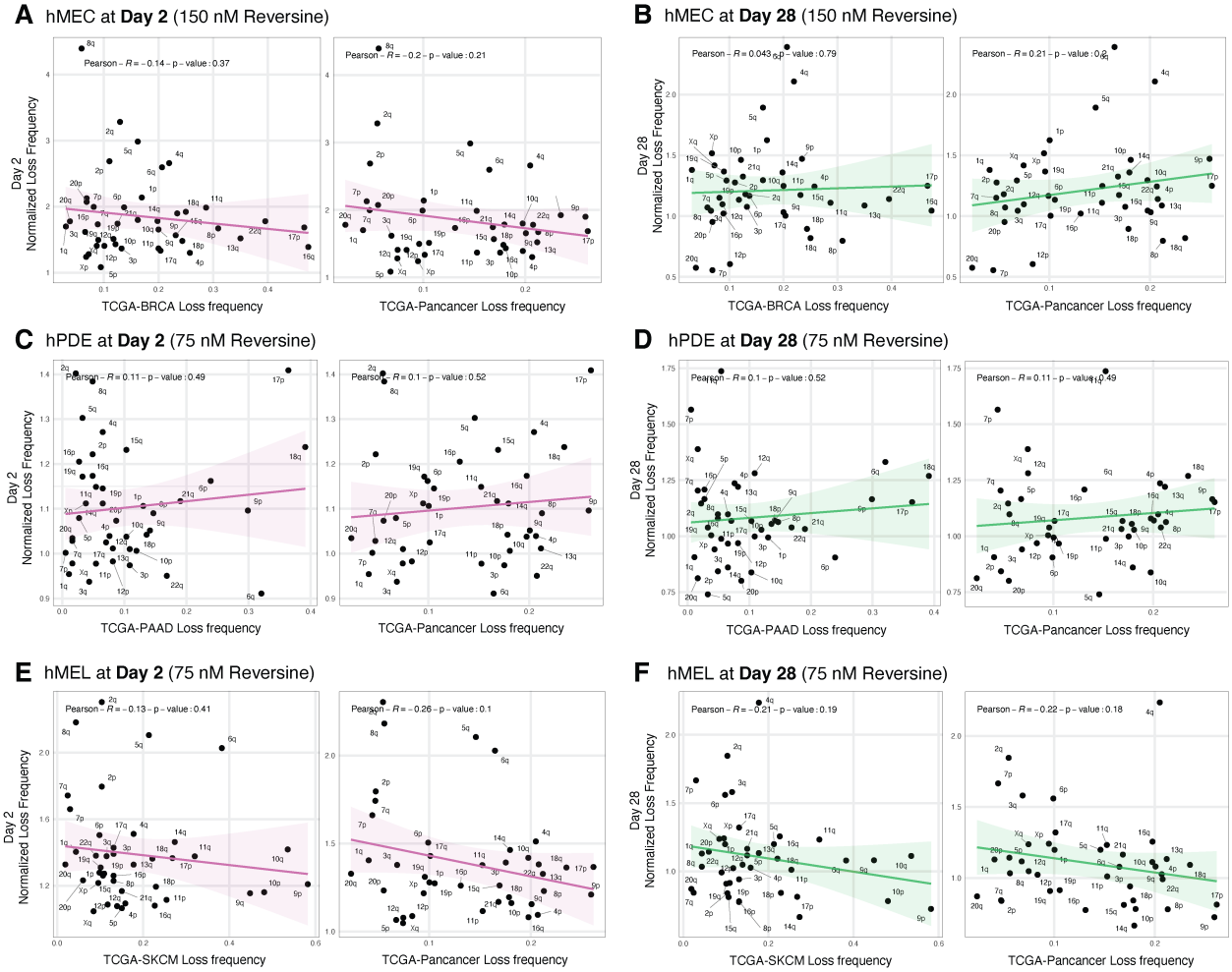

Supplementary Figure 11

Comparison of chromosome-arm loss frequencies induced by reversine with cancer amplification frequency from TCGA data. Panels compare normalized chromosome arm loss frequencies at Day 2 (A, C, E) and Day 28 (B, D, F) with TCGA deletion frequency from respective cancer types (hMEC with BRCA, hPDE with PAAD, and hMEL with SKCM) and Pancancer. Scatter plots include correlation coefficients (Pearson's R) and p-values. Green and pink regression lines distinguish between gains at Day 2 (pink) and Day 28 (green).

Supplementary Figure 12

karyotapR Workflow

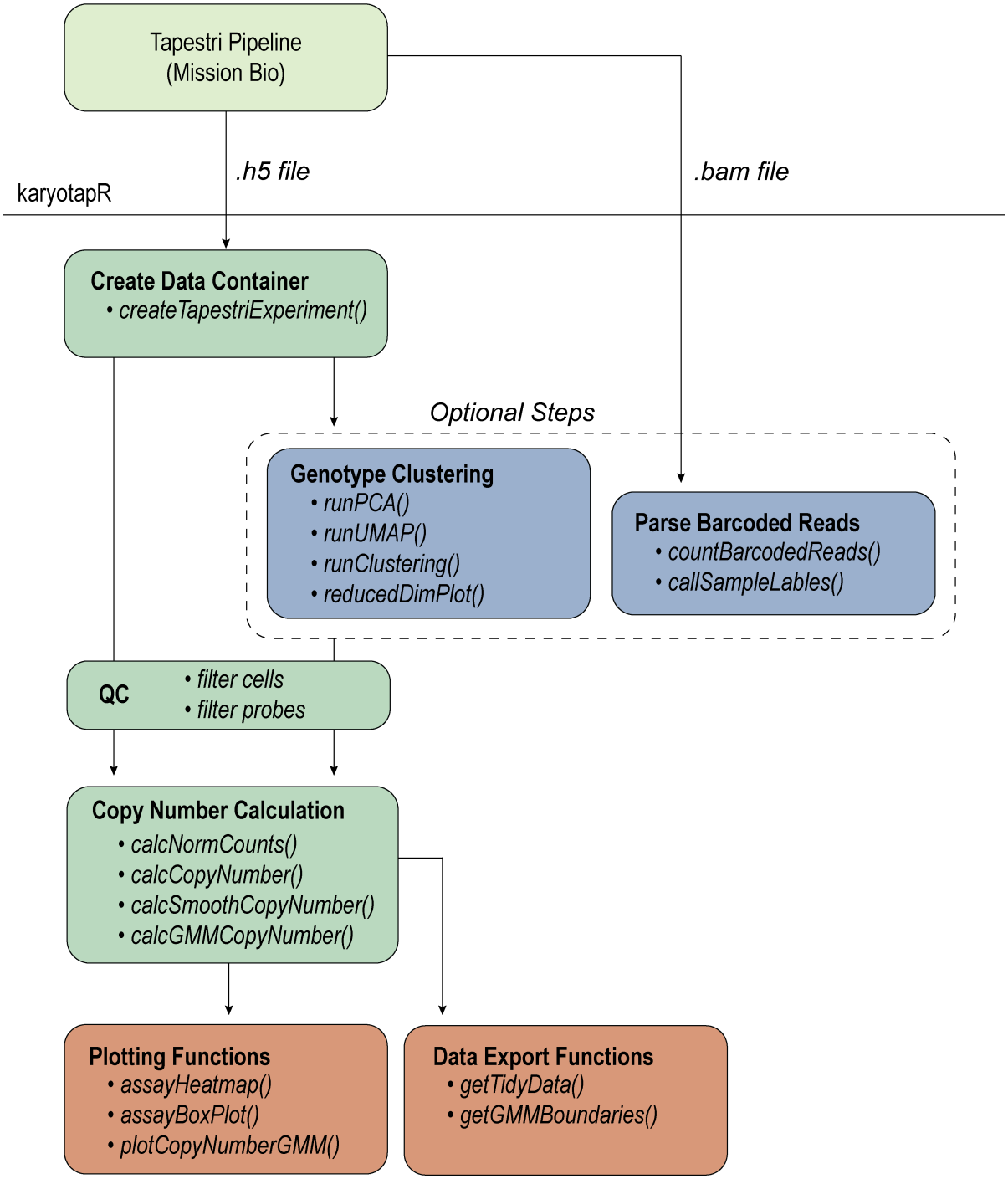

<u>Supplementary Figure 12</u>

Overview of workflow for copy number analysis using karyotapR R package.

1328 **Supplementary Table Legends**

1329

1330 **Supplementary Table 1**

1331 Number of probes per chromosome arm for custom Tapestri panels.

1332

1333 **Supplementary Table 2**

1334 Theoretical sensitivity of panel Version 1 copy number calls for each chromosome/chromosome arm at
1335 copy number values of 1, 2, 3, 4 and 5, calculated from GMMs.

1336

1337 **Supplementary Table 3**

1338 Theoretical sensitivity of panel Version 2 copy number calls for each chromosome/chromosome arm at
1339 copy number values of 1, 2, 3, 4 and 5, calculated from 5-component GMMs. “Gain” column indicates
1340 theoretical sensitivity for detecting chromosomal gains or ≥3 copies using 3-component GMM. 1 copy (5-
1341 component model) and “loss” detection (3-component model) sensitivities are equivalent. 2 copy (5-
1342 component model) and “neutral” detection (3-component model) sensitivities are equivalent.

1343

1344 **Supplementary Table 4**

1345 Sequences of barcodes and gRNAs.

1346

1347 **Supplementary Table 5**

1348 Results of Fisher’s exact test for chromosomal gains and losses induced by KaryoCreate. p-values from
1349 Fisher’s Exact test comparing the proportion of copy number gains and losses in each chromosome in
1350 each sample to the corresponding chromosome in the sgNC negative control sample are given.

1351

1352 **Supplementary Table 6**

1353 Percentage of chromosomal gains and losses Induced by KaryoCreate. Percentage indicates the
1354 proportion of cells in each KayroCreate-treated sample with either 1, 2, or 3+ copies of each
1355 chromosome.
1356
1357 **Supplementary Table 7**
1358 Theoretical sensitivity of panel Version 3 copy number calls for each chromosome/chromosome arm at
1359 copy number values of 1, 2, 3, 4 and 5, calculated from 5-component GMMs. “Gain” column indicates
1360 theoretical sensitivity for detecting chromosomal gains or ≥3 copies using 3-component GMM. 1 copy (5-
1361 component model) and “loss” detection (3-component model) sensitivities are equivalent. 2 copy (5-
1362 component model) and “neutral” detection (3-component model) sensitivities are equivalent.
1363
1364 **Supplementary Table 8**
1365 Sequences of barcodes used in the aneuploidy induction and in vitro screening experiment.
1366
1367

1368 **List of Abbreviations**

1369	BFP	Blue florescent protein
1370	CIN	Chromosomal instability
1371	CNV	Copy number variant
1372	DLP	Direct library preparation
1373	DOP-PCR	Degenerate-oligonucleotide-primed PCR
1374	FACS	Fluorescence associated cell sorting
1375	GMM	Gaussian mixture model
1376	gRNA	guide RNA
1377	hCECs	Human colorectal epithelial cells
1378	hPNEs	Human pancreatic nestin-expressing cells
1379	hMEC	Human mammary epithelial cells
1380	HMEL	Human Melanocytes
1381	hPDE	Human pancreatic duct epithelial cells
1382	MALBAC	Multiple annealing and looping-based amplification cycles
1383	MDA	Multiple displacement amplification
1384	MOI	Multiplicity of infection
1385	ORF	Open reading frame
1386	PCA	Principal components analysis
1387	PCR	Polymerase chain reaction
1388	PDF	Probability Density Function
1389	RPE1	Retinal pigment epithelial (cells) 1
1390	scDNA-seq	Single-cell DNA sequencing
1391	scRNA-seq	Single-cell RNA sequencing
1392	sgRNA	Single guide RNA
1393	SNP	Single-nucleotide polymorphism

SNV	Single nucleotide variant
VAF	Variant allele frequency
WGA	Whole genome amplification
WGS	Whole genome sequencing

1400 **Declarations**

1401

1402 **Ethics Approval and Consent to Participate**

1403 Not applicable

1404

1405 **Consent for Publication**

1406 Not applicable

1407

1408 **Availability of Data and Materials**

1409 Sequencing data for Tapestri experiments are available in the SRA repository under NCBI BioProject
1410 accession PRJNA950110, https://www.ncbi.nlm.nih.gov/bioproject/950110 (53). The karyotapR package
1411 is available on GitHub at http://github.com/joeymays/karyotapR (54).The source code for karyptapR
1412 version 0.1 used for this study is archived on Zenodo under DOI
1413 https://doi.org/10.5281/zenodo.8305561(55). All data analysis scripts used in this study are available at
1414 https://github.com/joeymays/karyotap-publication (56) and are archived on Zenodo under DOI
1415 https://doi.org/10.5281/zenodo.8329277. Tapestri Pipeline output files used in this study are available on
1416 Zenodo under DOI https://doi.org/10.5281/zenodo.8305841(57).

1417

1418 **Competing Interests**

1419 TD is on the Scientific Advisory Board of io9.

1420

1421 **Funding**

1422 LJH and GRK were supported by NIH R37 CA240765. TD was supported by the Cancer Research UK
1423 Grand Challenge and the Mark Foundation for Cancer Research (C5470/A27144), NIH R37
1424 R37CA248631, R01 R01HG012590, R01 R01DK135089, the MRA Young Investigator Award, the Breast

Cancer Alliance Young Investigator Award and a grant from The National Foundation for Cancer Research. FA was supported by an AICF postdoctoral fellowship.

Authors' contributions

JCM designed the study, performed wet lab experiments and bioinformatics analyses, developed the karyotapR software package, and wrote the manuscript for the KaryoTap development. FA design and performed experiments and bioinformatics analyses and wrote the manuscript for the in vitro screens. MT helped with the LOH analysis, experimental design and edited the manuscript. SM performed lentiviral preparation and transductions. NB and XZ designed Tapestri panels. JJB and HQ performed and supported cell culture. GRK prepared barcode vectors. LJH supervised research. TD designed the study, edited the manuscript, and supervised research.

Acknowledgments

NYU Langone's Genome Technology Center (RRID: SCR_017929) is supported by the Cancer Center Support Grant P30CA016087 at the Laura and Isaac Perlmutter Cancer Center. The computational requirements for this work were supported in part by the NYU Langone High Performance Computing (HPC) Core's resources and personnel. We thank Paolo Mita, Pan Cheng, and Lisa Katsnelson for their helpful suggestions and insights in the preparation of this work.

Competing Interests TD is co-founder of KaryoVerse Therapeutics and has stocks in Acurion Inc.

Additional Files

- AdditionalFile01.csv: Probe Design for Panel Version 1 (CO216)
- AdditionalFile02.csv: Probe Design for Panel Version 2 (CO610)
- AdditionalFile03.csv: Probe Design for Panel Version 3 (CO810)

1451 **References**

1452 1. Navin N, Krasnitz A, Rodgers L, Cook K, Meth J, Kendall J, et al. Inferring tumor progression from
1453 genomic heterogeneity. Genome Res. 2010 Jan;20(1):68–80.

1454 2. Ben-David U, Amon A. Context is everything: aneuploidy in cancer. Nature Reviews Genetics. 2020
1455 Jan;21(1):44–62.

1456 3. Weaver BAA, Cleveland DW. Aneuploidy: Instigator and Inhibitor of Tumorigenesis. Cancer
1457 Research. 2007 Nov 1;67(21):10103–5.

1458 4. Bakhoum SF, Ngo B, Laughney AM, Cavallo JA, Murphy CJ, Ly P, et al. Chromosomal instability
1459 drives metastasis through a cytosolic DNA response. Nature. 2018 Jan;553(7689):467–72.

1460 5. Bakhoum SF, Cantley LC. The Multifaceted Role of Chromosomal Instability in Cancer and Its
1461 Microenvironment. Cell. 2018 Sep 6;174(6):1347–60.

1462 6. Ippolito MR, Martis V, Martin S, Tijhuis AE, Hong C, Wardenaar R, et al. Gene copy-number
1463 changes and chromosomal instability induced by aneuploidy confer resistance to chemotherapy.
1464 Developmental Cell. 2021 Sep 13;56(17):2440-2454.e6.

1465 7. Lee AJX, Endesfelder D, Rowan AJ, Walther A, Birkbak NJ, Futreal PA, et al. Chromosomal
1466 Instability Confers Intrinsic Multidrug Resistance. Cancer Research. 2011 Mar 1;71(5):1858–70.

1467 8. Anagnostou V, Smith KN, Forde PM, Niknafs N, Bhattacharya R, White J, et al. Evolution of
1468 Neoantigen Landscape during Immune Checkpoint Blockade in Non–Small Cell Lung Cancer.
1469 Cancer Discovery. 2017 Mar 5;7(3):264–76.

1470 9. Lynch AR, Bradford S, Zhou AS, Oxendine K, Henderson L, Horner VL, et al. A survey of CIN
1471 measures across mechanistic models [Internet]. bioRxiv; 2023 [cited 2023 Aug 16]. p.
1472 2023.06.15.544840. Available from: https://www.biorxiv.org/content/10.1101/2023.06.15.544840v1

1473 10. Bakker B, Taudt A, Belderbos ME, Porubsky D, Spierings DCJ, de Jong TV, et al. Single-cell
1474 sequencing reveals karyotype heterogeneity in murine and human malignancies. Genome Biology.
1475 2016 May 31;17(1):115.

1476 11. Baslan T, Hicks J. Unravelling biology and shifting paradigms in cancer with single-cell sequencing.
1477 Nat Rev Cancer. 2017 Sep;17(9):557–69.

1478 12. Navin N, Kendall J, Troge J, Andrews P, Rodgers L, McIndoo J, et al. Tumour evolution inferred by
1479 single-cell sequencing. Nature. 2011 Apr;472(7341):90–4.

1480 13. Wang Y, Waters J, Leung ML, Unruh A, Roh W, Shi X, et al. Clonal evolution in breast cancer
1481 revealed by single nucleus genome sequencing. Nature. 2014 Aug;512(7513):155–60.

1482 14. Bosco N, Goldberg A, Zhao X, Mays JC, Cheng P, Johnson AF, et al. KaryoCreate: A CRISPR-
1483 based technology to study chromosome-specific aneuploidy by targeting human centromeres. Cell
1484 [Internet]. 2023 Apr 18 [cited 2023 Apr 20]; Available from:
1485 https://www.sciencedirect.com/science/article/pii/S0092867423003264

1486 15. Truong MA, Cané-Gasull P, de Vries SG, Nijenhuis W, Wardenaar R, Kapitein LC, et al. A kinesin-
1487 based approach for inducing chromosome-specific mis-segregation in human cells. The EMBO
1488 Journal. 2023 May 15;42(10):e111559.

1489 16. Tovini L, Johnson SC, Guscott MA, Andersen AM, Spierings DCJ, Wardenaar R, et al. Targeted
1490 assembly of ectopic kinetochores to induce chromosome-specific segmental aneuploidies. The
1491 EMBO Journal. 2023 May 15;42(10):e111587.

1492 17. Telenius H, Carter NP, Bebb CE, Nordenskjo¨ld M, Ponder BAJ, Tunnacliffe A. Degenerate
1493 oligonucleotide-primed PCR: General amplification of target DNA by a single degenerate primer.
1494 Genomics. 1992 Jul 1;13(3):718–25.

1495 18. Dean FB, Hosono S, Fang L, Wu X, Faruqi AF, Bray-Ward P, et al. Comprehensive human genome
1496 amplification using multiple displacement amplification. Proceedings of the National Academy of
1497 Sciences. 2002 Apr 16;99(8):5261–6.

1498 19. Zong C, Lu S, Chapman AR, Xie XS. Genome-Wide Detection of Single-Nucleotide and Copy-
1499 Number Variations of a Single Human Cell. Science. 2012 Dec 21;338(6114):1622–6.

1500 20. Mallory XF, Edrisi M, Navin N, Nakhleh L. Methods for copy number aberration detection from
1501 single-cell DNA-sequencing data. Genome Biology. 2020 Aug 17;21(1):208.

1502 21. Zahn H, Steif A, Laks E, Eirew P, VanInsberghe M, Shah SP, et al. Scalable whole-genome single-
1503 cell library preparation without preamplification. Nat Methods. 2017 Feb;14(2):167–73.

1504 22. Yin Y, Jiang Y, Lam KWG, Berletch JB, Disteche CM, Noble WS, et al. High-Throughput Single-Cell
1505 Sequencing with Linear Amplification. Molecular Cell [Internet]. 2019 Sep 5 [cited 2019 Sep 6];
1506 Available from: http://www.sciencedirect.com/science/article/pii/S1097276519306185

1507 23. Laks E, Zahn H, Lai D, McPherson A, Steif A, Brimhall J, et al. Resource: Scalable whole genome
1508 sequencing of 40,000 single cells identifies stochastic aneuploidies, genome replication states and
1509 clonal repertoires [Internet]. bioRxiv; 2018 [cited 2023 Jan 10]. p. 411058. Available from:
1510 https://www.biorxiv.org/content/10.1101/411058v2

1511 24. Evrony GD, Hinch AG, Luo C. Applications of Single-Cell DNA Sequencing. Annu Rev Genomics
1512 Hum Genet. 2021 Aug 31;22:171–97.

1513 25. Mission Bio. Mission Bio Tapestri. 2020 [cited 2020 May 7]. Tapestri: The Precision Genomics
1514 Platform. Available from: https://missionbio.com/tapestri/

1515 26. Gawad C, Koh W, Quake SR. Single-cell genome sequencing: current state of the science. Nat Rev
1516 Genet. 2016 Mar;17(3):175–88.

1517 27. Crasta K, Ganem NJ, Dagher R, Lantermann AB, Ivanova EV, Pan Y, et al. DNA breaks and
1518 chromosome pulverization from errors in mitosis. Nature. 2012 Feb;482(7383):53–8.

1519 28. Reijns MAM, Parry DA, Williams TC, Nadeu F, Hindshaw RL, Rios Szwed DO, et al. Signatures of
1520 TOP1 transcription-associated mutagenesis in cancer and germline. Nature. 2022
1521 Feb;602(7898):623–31.

1522 29. Aird D, Ross MG, Chen WS, Danielsson M, Fennell T, Russ C, et al. Analyzing and minimizing
1523 PCR amplification bias in Illumina sequencing libraries. Genome Biology. 2011 Feb 21;12(2):R18.

1524 30. Jothilakshmi S, Gudivada VN. Chapter 10 - Large Scale Data Enabled Evolution of Spoken
1525 Language Research and Applications. In: Gudivada VN, Raghavan VV, Govindaraju V, Rao CR,
1526 editors. Handbook of Statistics [Internet]. Elsevier; 2016 [cited 2023 Aug 22]. p. 301–40. (Cognitive
1527 Computing: Theory and Applications; vol. 35). Available from:
1528 https://www.sciencedirect.com/science/article/pii/S0169716116300463

1529 31. Knudson AG. Mutation and Cancer: Statistical Study of Retinoblastoma. Proceedings of the
1530 National Academy of Sciences. 1971 Apr;68(4):820–3.

1531 32. Shah JB, Pueschl D, Wubbenhorst B, Fan M, Pluta J, D'Andrea K, et al. Analysis of matched
1532 primary and recurrent BRCA1/2 mutation-associated tumors identifies recurrence-specific drivers.
1533 Nat Commun. 2022 Nov 7;13(1):6728.

1534 33. Ryland GL, Doyle MA, Goode D, Boyle SE, Choong DYH, Rowley SM, et al. Loss of
1535 heterozygosity: what is it good for? BMC Medical Genomics. 2015 Aug 1;8(1):45.

1536 34. Dong X, Zhang L, Hao X, Wang T, Vijg J. SCCNV: A Software Tool for Identifying Copy Number
1537 Variation From Single-Cell Whole-Genome Sequencing. Frontiers in Genetics [Internet]. 2020 [cited
1538 2023 Jun 2];11. Available from: https://www.frontiersin.org/articles/10.3389/fgene.2020.505441

1539 35. Shalem O, Sanjana NE, Zhang F. High-throughput functional genomics using CRISPR–Cas9. Nat
1540 Rev Genet. 2015 May;16(5):299–311.

1541 36. Ly P, Eskiocak U, Kim SB, Roig AI, Hight SK, Lulla DR, et al. Characterization of Aneuploid
1542 Populations with Trisomy 7 and 20 Derived from Diploid Human Colonic Epithelial Cells. Neoplasia.
1543 2011 Apr 1;13(4):348-IN17.

1544 37. Sherry ST, Ward MH, Kholodov M, Baker J, Phan L, Smigielski EM, et al. dbSNP: the NCBI
1545 database of genetic variation. Nucleic Acids Res. 2001 Jan 1;29(1):308–11.

1546 38. Nassar LR, Barber GP, Benet-Pagès A, Casper J, Clawson H, Diekhans M, et al. The UCSC
1547 Genome Browser database: 2023 update. Nucleic Acids Res. 2023 Jan 6;51(D1):D1188–95.

1548 39. Gel B, Serra E. karyoploteR: an R/Bioconductor package to plot customizable genomes displaying
1549 arbitrary data. Bioinformatics. 2017 Oct 1;33(19):3088–90.

1550 40. Bolger AM, Lohse M, Usadel B. Trimmomatic: a flexible trimmer for Illumina sequence data.
1551 Bioinformatics. 2014 Aug 1;30(15):2114–20.

1552 41. Li H. Aligning sequence reads, clone sequences and assembly contigs with BWA-MEM. 2013.

1553 42. Kuilman T, Velds A, Kemper K, Ranzani M, Bombardelli L, Hoogstraat M, et al. CopywriteR: DNA
1554 copy number detection from off-target sequence data. Genome Biol. 2015 Feb 27;16:49.

1555 43. Chen B, Gilbert LA, Cimini BA, Schnitzbauer J, Zhang W, Li GW, et al. Dynamic Imaging of
1556 Genomic Loci in Living Human Cells by an Optimized CRISPR/Cas System. Cell. 2013 Dec
1557 19;155(7):1479–91.

44. Ran FA, Hsu PD, Wright J, Agarwala V, Scott DA, Zhang F. Genome engineering using the CRISPR-Cas9 system. Nat Protoc. 2013 Nov;8(11):2281–308.

45. Sack LM, Davoli T, Li MZ, Li Y, Xu Q, Naxerova K, et al. Profound Tissue Specificity in Proliferation Control Underlies Cancer Drivers and Aneuploidy Patterns. Cell. 2018 Apr 5;173(2):499-514.e23.

46. Pagès H, Aboyoun P, Gentleman R, DebRoy S. Biostrings: Efficient manipulation of biological strings [Internet]. 2022. Available from: https://bioconductor.org/packages/Biostrings

47. Morgan M, Pagès H, Obenchain V, Hayden N. Rsamtools: Binary alignment (BAM), FASTA, variant call (BCF), and tabix file import [Internet]. 2022. Available from: https://bioconductor.org/packages/Rsamtools

48. Reijns MAM. WT1_ancestral_culture [Internet]. SRA; 2021 [cited 2023 Jan 18]. Available from: https://www.ncbi.nlm.nih.gov/sra/?term=ERR7477340

49. GATK [Internet]. [cited 2023 Mar 21]. Available from: https://gatk.broadinstitute.org/hc/en-us

50. Knaus BJ, Grünwald NJ. vcfr: a package to manipulate and visualize variant call format data in R. Molecular Ecology Resources. 2017;17(1):44–53.

51. Delignette-Muller ML, Dutang C. fitdistrplus: An R Package for Fitting Distributions. Journal of Statistical Software. 2015 Mar 20;64:1–34.

52. McCarthy DJ, Campbell KR, Lun ATL, Wills QF. Scater: pre-processing, quality control, normalization and visualization of single-cell RNA-seq data in R. Bioinformatics. 2017 Apr 15;33(8):1179–86.

53. Mays J, Davoli T. ID 950110 - BioProject - NCBI [Internet]. 2023 [cited 2023 Sep 12]. Available from: https://www.ncbi.nlm.nih.gov/bioproject/950110

54. Mays JC. karyotapR: CNV Analysis for Tapestri [Internet]. 2023 [cited 2023 Sep 8]. Available from: https://github.com/joeymays/karyotapR

55. Mays J. joeymays/karyotapR: Version 0.1 [Internet]. Zenodo; 2023 [cited 2023 Sep 8]. Available from: https://zenodo.org/record/8305561

56. Mays J. KaryoTap Publication Codebook [Internet]. 2023 [cited 2023 Sep 8]. Available from: https://github.com/joeymays/karyotap-publication

57. Mays J, Davoli T. KaryoTap Enables Aneuploidy Detection in Thousands of Single Human Cells [Internet]. Zenodo; 2023 [cited 2023 Sep 8]. Available from: https://zenodo.org/record/8305841

58. Davoli T, Xu AW, Mengwasser KE, Sack LM, Yoon JC, Park PJ, Elledge SJ. Cumulative haploinsufficiency and triplosensitivity drive aneuploidy patterns and shape the cancer genome. Cell. 2013 Nov 21;155(5):948-62.

59. Shih J, Sarmashghi S, Zhakula-Kostadinova N, Zhang S, Georgis Y, Hoyt SJ, Cucinotta CE, Schwartz C, Volkova O, Nurk S, Meredith M, Lajoie BR, Eng K, Shumate A, Gershman A, Rhie A, Soto DC, Perez GE, Miga KH, O'Neill RJ, Eichler EE, Sullivan BA, Phillippy AM, Mao JH, Pevzner PA, Alexandrov LB, Bafna V. Cancer aneuploid genomes exhibit distinctive mutational signatures.

Nature. 2023 Jun;618(7965):746-751.

60. Navin N, Kendall J, Troge J, Andrews P, Rodgers L, McIndoo J, Cook K, Stepansky A, Levy D, Esposito D, Muthuswamy L, Krasnitz A, McCombie WR, Hicks J, Wigler M. Tumour evolution inferred by single-cell sequencing. Nature. 2011 Apr;472(7341):90-4.

61. Baslan T, Kendall J, Rodgers L, Cox H, Riggs M, Stepansky A, Troge J, Ravi K, Esposito D, Lakshmi B, Wigler M, Navin N, Hicks J. Genome-wide copy number analysis of single cells. Nat Protoc. 2012 May;7(6):1024-41.

62. Mahlamäki EH, Bärlund M, Tanner M, Gorunova L, Höglund M, Karhu R, Kallioniemi A. Frequent amplification of 8q24, 11q, 17q, and 20q-specific genes in pancreatic cancer. Genes Chromosomes Cancer. 2002 Oct;35(4):353-8.

63. Hodgson JG, Chin K, Collins C, Gray JW. Genome amplification of chromosome 20 in breast cancer. Breast Cancer Res Treat. 2003 Apr;78(3):337-45.

64. Shoshani O, Brunner SF, Yaeger R, Ly P, Nechemia-Arbely Y, Kim DH, Fang R, Castillon GA, Yu M, Li JSZ, Sun Y, Ellisman MH, Ren B, Pevzner PA, Dixon JR, Misteli T, Stephens PJ, Cleveland DW. Chromothripsis drives the evolution of gene amplification in cancer. Nature. 2021 Mar;591(7848):137-141.

65. Dumont M, Gamba R, Gestraud P, Klaasen S, Worrall JT, De Vries SG, Boudreau V, Salinas-Luypaert C, Maddox PS, Lens SM, Kops GJ, McClelland SE, Miga KH, Fachinetti D. Human chromosome-specific aneuploidy is influenced by DNA-dependent centromeric features. EMBO J. 2020 Jan 15;39(2):e102924.

66. Hwang KT, Han W, Cho J, Lee JW, Ko E, Kim EK, Jung SY, Jeong EM, Bae JY, Kang JJ, Yang SJ, Kim SW, Noh DY. Genomic copy number alterations as predictive markers of systemic recurrence in breast cancer. Int J Cancer. 2008 Oct;123(8):1807-15.

67. Sack LM, Davoli T, Li MZ, Li Y, Xu Q, Naxerova K, Wooten EC, Bernardi RJ, Martin TD, Chen T, Leng K, Liang AC, Scorsone KA, Westbrook TF, Wong KK, Elledge SJ. Profound Tissue Specificity in Proliferation Control Underlies Cancer Drivers and Aneuploidy Patterns. Cell. 2018 Apr;173(2):499-514.e23.

68. Rama Ballesteros AR, Hernández R, Perazzoli G, Cabeza L, Melguizo C, Vélez C, Prados J. Specific driving of the suicide E gene by the CEA promoter enhances the effects of paclitaxel in lung cancer. Cancer Gene Ther. 2020 Sep;27(9):657-668.

69. Klaasen SJ, Truong MA, van Jaarsveld RH, Koprivec I, Štimac V, de Vries SG, Risteski P, Kodba S, Vukušić K, de Luca KL, Marques JF, Gerrits EM, Bakker B, Foijer F, Kind J, Tolić IM, Lens SMA, Kops GJPL. Nuclear chromosome locations dictate segregation error frequencies. Nature. 2022 Jul;607(7919):604-609.

70. Lin Y, Wang J, Wang K, Bai S, Thennavan A, Wei R, Yan Y, Li J, Elgamal H, Sei E, Casasent A, Rao M, Tang C, Multani AS, Ma J, Montalvan J, Nagi C, Winocour S, Lim B, Thompson A, Navin N. Normal breast tissues harbour rare populations of aneuploid epithelial cells. Nature. 2024 Dec;636(8043):663-670.

71. Ciani Y, Fedrizzi T, Prandi D, Lorenzin F, Locallo A, Gasperini P, Franceschini GM, Benelli M,

Elemento O, Fava LL, Inga A, Demichelis F. Allele-specific genomic data elucidate the role of somatic gain and copy-number neutral loss of heterozygosity in cancer. Cell Syst. 2022 Feb;13(2):183–193.e7.

72. Watson EV, Lee JJ-K, Gulhan DC, Melloni GEM, Venev SV, Magesh RY, Frederick A, Chiba K, Wooten EC, Naxerova K, Dekker J, Park PJ, Elledge SJ. Chromosome evolution screens recapitulate tissue-specific tumor aneuploidy patterns. Nat Genet. 2024 May;56(5):900–912.

73. Jubran J, Slutsky R, Rozenblum N, Rokach L, Ben-David U, Yeger-Lotem E. Machine-learning analysis reveals an important role for negative selection in shaping cancer aneuploidy landscapes. Genome Biol. 2024 Apr 15;25(1):95.

74. Santaguida S, Tighe A, D'Alise AM, Taylor SS, Musacchio A. Dissecting the role of MPS1 in chromosome biorientation and the spindle checkpoint through the small molecule inhibitor reversine. J Cell Biol. 2010 Jul 26;190(1):73-87

75. Williams MJ, Oliphant MUJ, Chen Z, Fowler JC, McFarland JM, Ben-David U. Luminal breast epithelial cells of BRCA1 or BRCA2 mutation carriers and noncarriers harbor common breast cancer copy number alterations. Nat Genet. 2024 Dec;56(12):2753–2762.

76. Davoli T, Uno H, Wooten EC, Elledge SJ. Tumor aneuploidy correlates with markers of immune evasion and with reduced response to immunotherapy. Science. 2017 Jan 20;355(6322):eaaf8399.

77. Alfieri F, Senger G, Oliveto G, Kogenaru M, Davoli T, Schaefer M. Explainable machine learning reveals forces acting on amplifications and deletions across cancer genomes. Back-to-back submission, 2025.

78. Karlsson K, Przybilla MJ, Kotler E, Xu H, Ma Z, Liu K, Curtis C. Deterministic evolution and stringent selection during preneoplasia. Nature. 2023 Jun;618(7937):383–393